Inverse Problems and Imaging doi:10.3934/ipi.2016.10.195
Volume 10, No. 1, 2016, 195–225

PRECONDITIONED CONJUGATE GRADIENT METHOD FOR BOUNDARY ARTIFACT-FREE IMAGE DEBLURRING

Nam-Yong Lee*

Department of Applied Mathematics
Inje University
Gimhae, Gyeongnam 621-749, Korea

Bradley J. Lucier

Department of Mathematics
Purdue University
West Lafayette, IN47906, USA

(Communicated by Hao-Min Zhou)

Abstract. Several methods have been proposed to reduce boundary artifacts in image deblurring. Some of those methods impose certain assumptions on image pixels outside the field-of-view; the most important of these assume reflective or anti-reflective boundary conditions. Boundary condition methods, including reflective and anti-reflective ones, however, often fail to reduce boundary artifacts, and, in some cases, generate their own artifacts, especially when the image to be deblurred does not accurately satisfy the imposed condition. To overcome these difficulties, we suggest using *free boundary conditions*, which do not impose any restrictions on image pixels outside the field-of-view, and *preconditioned conjugate gradient methods*, where preconditioners are designed to compensate for the non-uniformity in contributions from image pixels to the observation. Our simulation studies show that the proposed method outperforms reflective and anti-reflective boundary condition methods in removing boundary artifacts. The simulation studies also show that the proposed method can be applicable to arbitrarily shaped images and has the benefit of recovering damaged parts in blurred images.

1. Introduction.

1.1. The problem of deblurring.

For an image $\mathbf{f} = (f_{j_1,j_2})$ defined for (j_1, j_2) in some rectangular domain Ω, we assume that we can observe only a noisy, blurred image

$$\mathbf{g} = \mathcal{T}\mathbf{f} + \mathbf{n}. \tag{1}$$

Here $\mathcal{T}$, sometimes called a *projector*, is a linear transform that determines the blurring process acting on the image $\mathbf{f}$. We assume that $\mathcal{T}$ can be expressed as a *truncated convolution* with a point spread function (PSF) $\mathbf{k} = (k_{j_1,j_2})$,

$$(\mathcal{T}\mathbf{f})_{i_1,i_2} = \sum_{(j_1,j_2)\in\operatorname{supp}\mathbf{k}} k_{j_1,j_2} f_{i_1-j_1,i_2-j_2}. \tag{2}$$

2010 *Mathematics Subject Classification.* Primary: 65F08, 65K10, 68U10.
Key words and phrases. Boundary artifacts, image deblurring, convolution, preconditioner.

* Corresponding author.

Here $\operatorname{supp}\mathbf{k}$, the *support* of $\mathbf{k}$, is $\{(j_1,j_2) \mid k_{j_1,j_2} > 0\}$. The PSF $\mathbf{k}$ is nonnegative, its components have sum 1, and the point $(0,0) \in \operatorname{supp}\mathbf{k}$; $\mathcal{T}\mathbf{f}$ is defined on Λ, where $(i_1,i_2) \in \Lambda$ if and only if $(i_1,i_2) - \operatorname{supp}\mathbf{k} \subseteq \Omega$.

So $\mathcal{T}\colon L^2(\Omega) \to L^2(\Lambda)$; the notation $L^2(\Omega)$ is the inner product space equipped with the inner product defined by

$$\langle \mathbf{p}, \tilde{\mathbf{p}}\rangle = \sum_{(j_1,j_2)\in\Omega} p_{j_1,j_2}\tilde{p}_{j_1,j_2}$$

for any images $\mathbf{p}$ and $\tilde{\mathbf{p}}$ that are defined on Ω. We sometimes use a *weighted* inner product on Ω; the notation $L^2(\Omega,\mathbf{w})$ means the space equipped with the weighted inner product defined by

$$\langle \mathbf{p}, \tilde{\mathbf{p}}\rangle_{\mathbf{w}} = \sum_{(j_1,j_2)\in\Omega} p_{j_1,j_2}\tilde{p}_{j_1,j_2}w_{j_1,j_2}, \tag{3}$$

where the *weight* $\mathbf{w} = (w_{j_1,j_2})$ is defined on Ω.

The result $\mathcal{T}\mathbf{f}$ is further contaminated by noise $\mathbf{n}$, which we assume to be independent and identically distributed mean zero Gaussian.

Note that $\mathcal{T}$ is not an invertible operator—there are more pixels in $\mathbf{f}$ than there are in $\mathcal{T}\mathbf{f}$.

The deblurring problem is: Assuming that we have data $\mathbf{g}$, observed from a true image $\mathbf{f}$ by the observation model (1), determine an approximation $\hat{\mathbf{f}}$ to $\mathbf{f}$. Because $\mathcal{T}$ is not invertible, this problem is *ill posed*.

1.2. Previous work: Minimizing boundary artifacts.

In many imaging environments, the noise and the blurring are unavoidable phenomena, due to various reasons such as intrinsic or malfunctioned imaging system, movements of objects to be imaged, intrinsic limitation in measurement, etc. The task of image deblurring is to recover a sharp original image from its noisy, blurred version. Examples of image deblurring include motion deblurring for camera shake, satellite imaging, astronomical telescope, microscopy, and medical imaging, etc [12].

Much attention has been given to the general deblurring problem, and researchers have developed many techniques to approach this problem because there are a number of obstacles to obtaining satisfactory solutions, see [19]. From among these obstacles, we focus here mainly on the problem of *boundary artifacts* [12].

Some authors have used so-called *boundary condition* methods [15, 18, 7, 8]. In these methods, it is assumed for computational purposes that f_{j_1,j_2} in $\Omega - \Lambda$ is related to $\mathbf{f}$ in Λ via a fixed formula. Among boundary condition methods, we shall compare our method with *reflective* and *anti-reflective* boundary condition methods. To do so, we assume that the *extension operator* $\mathbb{E}\colon L^2(\Lambda) \to L^2(\Omega)$ satisfies $(\mathbb{E}\mathbf{f})_{j_1,j_2} = f_{j_1,j_2}$ for $(j_1,j_2) \in \Lambda$. Outside Λ, $\mathbf{f}$ is extended either *symmetrically* (these are reflective boundary conditions) or *anti-symmetrically* (these are anti-reflective boundary conditions); precise definitions will be given later.

To deal with the ill-posed-ness of image deblurring problem, boundary condition methods often use the Tikhonov regularization approach that finds $\hat{\mathbf{f}}$ that minimizes over all $\mathbf{q} \in L^2(\Lambda)$

$$\|\mathbf{g} - \mathcal{T}\mathbb{E}\mathbf{q}\|^2_{L^2(\Lambda)} + \lambda\|\mathbf{q}\|^2_{L^2(\Lambda)}, \tag{4}$$

where λ is a positive *regularization* parameter.

Some authors have suggested that not imposing a boundary condition may lead to a better reconstruction $\hat{\mathbf{f}}$ [5, 20, 6, 2]. We call this a *free boundary* method;

Calvetti *et al.* calls this an *Aristotelian* approach [6] and Almeida *et al.* calls this an *unknown boundary condition* [2]. To deal with the ill-posed-ness of image deblurring problem, we combine the free boundary condition with Tikhonov regularization to find $\hat{\mathbf{f}}$ that minimizes over all $\mathbf{p} \in L^2(\Omega)$

$$\|\mathbf{g} - \mathcal{T}\mathbf{p}\|^2_{L^2(\Lambda)} + \lambda\|\mathbf{p}\|^2_{L^2(\Omega)}. \tag{5}$$

Later, we shall propose to put a weight $\mathbf{w}$ on the domain Ω, and so consider the space $L^2(\Omega, \mathbf{w})$.

In all these cases, Tikhonov regularization leads to a linear problem, which can be written in general in the form of *normal equations*

$$\mathcal{A}\mathbf{x} = \mathbf{y}, \tag{6}$$

where $\mathcal{A}$ is a positive definite operator and $\mathbf{x}$ is the minimizer of either (4) or (5) (with either $L^2(\Omega)$ or $L^2(\Omega, \mathbf{w})$). In practice, it is important that these normal equations are *not* solved exactly; most practitioners use iterative methods, often Conjugate Gradient, with a small number of iterations.

In this paper we consider an incompletely-iterated Conjugate Gradient (CG) method to find an approximate solution to these equations. Mathematically, if there are N iterations of the CG method, then the image that approximately solves (6) is

$$\hat{\mathbf{x}} = \Pi^{\mathcal{A}}_{\mathrm{span}\{\mathbf{y}, \mathcal{A}\mathbf{y}, \ldots, \mathcal{A}^N\mathbf{y}\}} \mathcal{A}^{-1}\mathbf{y}, \tag{7}$$

where $\Pi^{\mathcal{A}}_{\mathcal{X}}\mathbf{h}$ is the projection of $\mathbf{h}$ onto the space $\mathcal{X}$ with the inner product defined as $\langle \mathbf{u}, \mathbf{v}\rangle_{\mathcal{A}} = \langle \mathbf{u}, \mathcal{A}\mathbf{v}\rangle$.

1.3. **Our approach.** We combine a number of previous approaches to this problem. In particular, we propose combining Tikhonov regularization, free boundary conditions, and incomplete CG iterations. To be specific, we propose the Tikhonov regularization to find $\hat{\mathbf{f}}$ that minimizes over all $\mathbf{p} \in L^2(\Omega, \mathbf{w})$

$$\|\mathbf{g} - \mathcal{T}\mathbf{p}\|^2_{L^2(\Lambda)} + \lambda\|\mathbf{p}\|^2_{L^2(\Omega, \mathbf{w})}; \tag{8}$$

here $\mathbf{w} = \mathcal{T}^*\mathbf{I}_\Lambda$, where $\mathcal{T}^*$ is the adjoint operator of $\mathcal{T}$ and $\mathbf{I}_{\mathcal{X}}$ is the image of all 1s on $\mathcal{X}$. Thus, the suggested normal equation is

$$(\mathcal{T}^*\mathcal{T} + \lambda\mathcal{W})\,\mathbf{p} = \mathcal{T}^*\mathbf{g}, \tag{9}$$

or

$$\mathcal{A}\mathbf{x} = \mathbf{y}, \quad \text{where } \mathcal{A} = \mathcal{T}^*\mathcal{T} + \lambda\mathcal{W},\ \mathbf{y} = \mathcal{T}^*\mathbf{g}, \text{ and } \mathbf{x} = \mathbf{p}; \tag{10}$$

here $\mathcal{W}$ is the diagonal operator defined by the the weight $\mathbf{w}$, that is, $\mathcal{W}\mathbf{p} = \mathbf{w} .\!* \mathbf{p}$ for $\mathbf{p} \in L^2(\Omega, \mathbf{w})$, where $.*$ is the pixel-by-pixel multiplication.

Additionally, we shall find that a better reconstruction occurs when we *precondition* the CG iteration with $\mathcal{W}$. Mathematically, this is equivalent to applying *un-preconditioned* CG iterations to the modified problem

$$[\mathcal{W}^{-1/2}\,(\mathcal{T}^*\mathcal{T} + \lambda\mathcal{W})\,\mathcal{W}^{-1/2}](\mathcal{W}^{1/2}\mathbf{p}) = \mathcal{W}^{-1/2}\mathcal{T}^*\mathbf{g} \tag{11}$$

or

$$\tilde{\mathcal{A}}\tilde{\mathbf{x}} = \tilde{\mathbf{y}}, \tag{12}$$

where $\tilde{\mathbf{y}} = \mathcal{W}^{-1/2}\mathcal{T}^*\mathbf{g}$, $\tilde{\mathcal{A}} = \mathcal{W}^{-1/2}\,(\mathcal{T}^*\mathcal{T} + \lambda\mathcal{W})\,\mathcal{W}^{-1/2}$, and $\tilde{\mathbf{x}} = \mathcal{W}^{1/2}\mathbf{p}$.

We have the relationship $\mathbf{x} = \mathcal{W}^{-1/2}\tilde{\mathbf{x}}$. However, after N iterations, preconditioned CG computes the image

$$\mathcal{W}^{-1/2}\Pi^{\tilde{\mathcal{A}}}_{\mathrm{span}\{\mathcal{W}^{-1/2}\mathcal{T}^*\mathbf{g},\tilde{\mathcal{A}}\mathcal{W}^{-1/2}\mathcal{T}^*\mathbf{g},\ldots,\tilde{\mathcal{A}}^N\mathcal{W}^{-1/2}\mathcal{T}^*\mathbf{g}\}}\tilde{\mathcal{A}}^{-1}\mathcal{W}^{-1/2}\mathcal{T}^*\mathbf{g}, \tag{13}$$

which is in general different from the image computed without preconditioning

$$\Pi^{\mathcal{A}}_{\mathrm{span}\{\mathcal{T}^*\mathbf{g},\mathcal{A}\mathcal{T}^*\mathbf{g},\ldots,\mathcal{A}^N\mathbf{y}\}}\mathcal{A}^{-1}\mathcal{T}^*\mathbf{g}. \tag{14}$$

In this paper, the proposed preconditioner $\mathcal{W}$ is specifically designed for the suppression of boundary artifacts, not for the acceleration of iterations. We shall show that the combination of free boundary conditions and the preconditioner $\mathcal{W}$ can suppress boundary artifacts more effectively than other boundary condition methods, especially in CG iterations associated with the Tikhonov regularization.

1.4. Outline.

This paper is outlined as follows. In Section 2 we review notation, terminology, and background material, including reflective and anti-reflective boundary conditions. In Section 3 we suggest free boundary conditions and preconditioned CG iteration as a method for boundary artifact removal. In Section 4 we present simulation results of the proposed method with comparison to methods using reflective and anti-reflective boundary conditions, and applications of the proposed method. Finally, we present some discussion and conclusions in Section 5.

2. Background.

2.1. Notation and terminology.

In this paper, we shall use following notations, conventions, and terminology.

- $\mathbf{g} = \mathcal{T}\mathbf{f} + \mathbf{n}$: the observation model, where $\mathbf{f}$ is the true image to be recovered, $\mathcal{T}$ is the projector that represents the space-invariant blurring of a given problem, $\mathbf{g}$ is the observed image, and $\mathbf{n}$ is Gaussian noise.
- $\mathbf{f} = (f_{j_1,j_2})$: the image, $\mathbf{f}$, will be denoted in a bold-faced alphabet, while its image pixel value, f_{j_1,j_2} at (j_1, j_2), will be denoted in a normal alphabet with subscripted indices. The same rule will hold for other images and PSFs throughout this paper.
- Λ: the set of image pixels where $\mathbf{g}$ is defined.
- Ω: the set of image pixels where $\mathbf{f}$ is defined.
- $\Omega - \Lambda$: the set of *"unseen" image pixels* across the boundary of Λ.
- $L^2(\Lambda)$: the set of images defined on Λ; for instance, $\mathbf{g} \in L^2(\Lambda)$.
- $L^2(\Omega)$: the set of images defined on Ω; for instance, $\mathbf{f} \in L^2(\Omega)$.
- $\mathcal{I}_\Lambda$: the identity map on the image space defined on Λ.
- $\mathcal{I}_\Omega$: the identity map on the image space defined on Ω.
- $\mathbf{I}_\Theta$: the all-one image on a pixel set $\Theta \subseteq \Lambda$ (or Ω),

$$(\mathbf{I}_\Theta)_{i_1,i_2} = \begin{cases} 1, & \text{if } (i_1, i_2) \in \Theta, \\ 0, & \text{if } (i_1, i_2) \notin \Theta. \end{cases} \tag{15}$$

- $\mathbf{k}$: the PSF that defines the projector $\mathcal{T}$ by (2).
- $\bar{\mathbf{k}}$: the reverse ordered PSF of $\mathbf{k} = (k_{i_1,i_2})$,

$$\bar{\mathbf{k}} = (\bar{k}_{i_1,i_2}) \text{ and } \bar{k}_{i_1,i_2} = k_{-i_1,-i_2}. \tag{16}$$

- $\operatorname{supp}\mathbf{k}$: the support of $\mathbf{k}$, the set of (i_1, i_2) such that $k_{i_1,i_2} \neq 0$.

- Standard backprojector $\mathcal{T}^*$: the adjoint transform $\mathcal{T}^*\colon L^2(\Lambda) \to L^2(\Omega)$ associated with the projector $\mathcal{T}\colon L^2(\Omega) \to L^2(\Lambda)$, which is uniquely determined by the relation

$$(\mathbf{q}, \mathcal{T}\mathbf{p}) = \langle \mathcal{T}^*\mathbf{q}, \mathbf{p}\rangle, \tag{17}$$

  for all $\mathbf{q} \in L^2(\Lambda)$ and $\mathbf{p} \in L^2(\Omega)$. Here $(\cdot,\cdot)$ and $\langle\cdot,\cdot\rangle$ are the inner products of two images in $L^2(\Lambda)$ and $L^2(\Omega)$, respectively.

Throughout this paper, we assume that the PSF $\mathbf{k}$ is non-negative with positive origin,

$$k_{i_1,i_2} \geq 0 \text{ and } k_{0,0} > 0, \tag{18}$$

and normalized to 1, i.e.,

$$\sum_{(i_1,i_2)\in \operatorname{supp}\mathbf{k}} k_{i_1,i_2} = 1. \tag{19}$$

2.2. **Projector and backprojector.** The relation between the PSF $\mathbf{k}$ and the projector $\mathcal{T}$ is defined by (2). In this paper, the right hand side of (2) will be denoted by $\mathbf{k} *_V \mathbf{f}$, i.e.,

$$\mathcal{T}\mathbf{p} = \mathbf{k} *_V \mathbf{p} \quad \text{for all } \mathbf{p} \in L^2(\Omega), \tag{20}$$

and called the *valid convolution* of $\mathbf{k}$ and $\mathbf{f}$. For future use, let the *full convolution* of $\bar{\mathbf{k}}$ and $\mathbf{q}$ in $L^2(\Lambda)$ be defined by

$$(\bar{\mathbf{k}} *_F \mathbf{q})_{j_1,j_2} = \sum_{(i_1,i_2)\in \operatorname{supp}\mathbf{k}\cap((j_1,j_2)+\Lambda)} k_{i_1,i_2} q_{i_1-j_1,i_2-j_2}. \tag{21}$$

Here $(\bar{\mathbf{k}} *_F \mathbf{q})_{j_1,j_2}$ is defined for (j_1, j_2) if and only if $\operatorname{supp}\mathbf{k} \cap ((j_1, j_2) + \Lambda) \neq \emptyset$.

In the previous section, we defined Ω to be the set of image pixels where the true image $\mathbf{f}$ is defined. Since we cannot recover $\mathbf{f}$ on image pixels that do not give any contribution to the observed image $\mathbf{g}$, we can redefine Ω to be the set of image pixels that actually contribute to the observed image $\mathbf{g}$ through the blurring by the PSF $\mathbf{k}$. Following this rule, we have

$$\Omega = \{(j_1, j_2) \mid (\bar{\mathbf{k}} *_F \mathbf{I}_\Lambda)_{j_1,j_2} > 0\}. \tag{22}$$

Here we note that this result implies $\Lambda \subset \Omega$, since $k_{0,0} > 0$. The proof of (22) immediately follows from the definition of the full convolution.

Previously, we defined the standard backprojector $\mathcal{T}^*$ abstractly by the basic theory of linear algebra. When $\mathcal{T}$ is defined by the valid convolution by the PSF $\mathbf{k}$, a more practical definition of the standard backprojector $\mathcal{T}^*$ is based on following result:

$$(\forall \mathbf{p} \in L^2(\Omega)) \quad \mathcal{T}\mathbf{p} = \mathbf{k} *_V \mathbf{p} \Longleftrightarrow (\forall \mathbf{q} \in L^2(\Lambda)) \quad \mathcal{T}^*\mathbf{q} = \bar{\mathbf{k}} *_F \mathbf{q}. \tag{23}$$

The proof of (23) also immediately follows from the definition of valid and full convolutions.

The computation of $\mathcal{T}\mathbf{p}$ (or $\mathbf{k} *_V \mathbf{p}$) and $\mathcal{T}^*\mathbf{q}$ (or $\bar{\mathbf{k}} *_F \mathbf{q}$) can be performed either by pixel-wise definitions (2) and (21) or by the fast Fourier transform (FFT) with zero-paddings. Pixel-wise computations are preferred for PSFs with small support, while FFT-based computations are needed for PSFs with large support.

2.3. **Boundary condition methods.** In this section, we shall explain three boundary conditions (reflective, anti-reflective, and free), which have been studied by many researchers [5, 15, 18, 7, 8, 6].

To present reflective and anti-reflective boundary conditions, we assume that

$$\Lambda = \{(i_1, i_2) \mid 0 \le i_\nu < N_\nu \ (\nu = 1, 2)\} \tag{24}$$

for some positive integers N_1 and N_2. To avoid some technical difficulty, we also assume that

$$\operatorname{supp} \mathbf{k} = \{(i_1, i_2) \mid -L_\nu \le i_\nu \le M_\nu \ (\nu = 1, 2)\} \tag{25}$$

for some positive integers L_1, L_2, M_1, and M_2. In this case,

$$\Omega = \{(j_1, j_2) \mid -M_\nu \le j_\nu \le N_\nu + L_\nu - 1 \ (\nu = 1, 2)\}. \tag{26}$$

We divide the true image $\mathbf{f}$ into 9 parts as follows:

$$\mathbf{f} = \begin{pmatrix} \mathbf{f}_{nw} & \mathbf{f}_n & \mathbf{f}_{ne} \\ \mathbf{f}_w & \mathbf{f}_c & \mathbf{f}_e \\ \mathbf{f}_{sw} & \mathbf{f}_s & \mathbf{f}_{se} \end{pmatrix}, \tag{27}$$

where $\mathbf{f}_c = (f_{i_1, i_2})$, $0 \le i_\nu < N_\nu$ $(\nu = 1, 2)$ represents the image part defined on Λ; each of the other eight parts, $\mathbf{f}_{nw}$, $\mathbf{f}_n$, $\mathbf{f}_{ne}$, $\mathbf{f}_w$, $\mathbf{f}_e$, $\mathbf{f}_{sw}$, $\mathbf{f}_s$, and $\mathbf{f}_{se}$ in (27), represents part of the image defined on $\Omega - \Lambda$, the set of unseen image pixels across the boundary of Λ.

Boundary condition methods impose certain restrictions on $\mathbf{f}_{nw}$, $\mathbf{f}_n$, $\mathbf{f}_{ne}$, $\mathbf{f}_w$, $\mathbf{f}_e$, $\mathbf{f}_{sw}$, $\mathbf{f}_s$, and $\mathbf{f}_{se}$ in (27). For example, the i-th row of the reflective boundary condition imposed image is

$$\begin{aligned} (&f_{i,M_2-1}, \cdots, f_{i,1}, f_{i,0}, \\ &\quad f_{i,0}, f_{i,1}, \cdots, f_{i,N_2-2}, f_{i,N_2-1}, \\ &\qquad f_{i,N_2-1}, f_{i,N_2-2}, \cdots, f_{i,N_2-L_2}), \end{aligned} \tag{28}$$

and similarly for the column, while the i-th row of the anti-reflective boundary condition imposed image is

$$\begin{aligned} (&2f_{i,0} - f_{i,M_2}, \cdots, 2f_{i,0} - f_{i,2}, 2f_{i,0} - f_{i,1}, \\ &\quad f_{i,0}, f_{i,1}, \cdots, f_{i,N_2-1}, f_{i,N_2-1}, \\ &\qquad 2f_{i,N_2-1} - f_{i,N_2-2}, \cdots, 2f_{i,N_2-1} - f_{i,N_2-L_2-1}), \end{aligned} \tag{29}$$

and similarly for the column. Figure 1 illustrates periodic (a), reflective (b), and anti-reflective (c) boundary conditions that extend images across upper and left boundaries.

Any set of boundary conditions introduces an *extension operator* $\mathbb{E}\colon L^2(\Lambda) \to L^2(\Omega)$ such that

$$\mathbb{E}\mathbf{f}_c = \begin{pmatrix} \tilde{\mathbf{f}}_{nw} & \tilde{\mathbf{f}}_n & \tilde{\mathbf{f}}_{ne} \\ \tilde{\mathbf{f}}_w & \mathbf{f}_c & \tilde{\mathbf{f}}_e \\ \tilde{\mathbf{f}}_{sw} & \tilde{\mathbf{f}}_s & \tilde{\mathbf{f}}_{se} \end{pmatrix}, \tag{30}$$

where $\tilde{\mathbf{f}}_{nw}$, $\tilde{\mathbf{f}}_n$, $\tilde{\mathbf{f}}_{ne}$, $\tilde{\mathbf{f}}_w$, $\tilde{\mathbf{f}}_e$, $\tilde{\mathbf{f}}_{sw}$, $\tilde{\mathbf{f}}_s$, and $\tilde{\mathbf{f}}_{se}$ represent parts of the image imposed by the boundary condition. The operators $\mathbb{E}$ associated with reflective and anti-reflective boundary conditions can be defined by (28) and (29), respectively.

In [15, 18, 7], reflective and anti-reflective boundary condition methods take the form (4) as Tikhonov regularization [9]. In this work, to test the performance

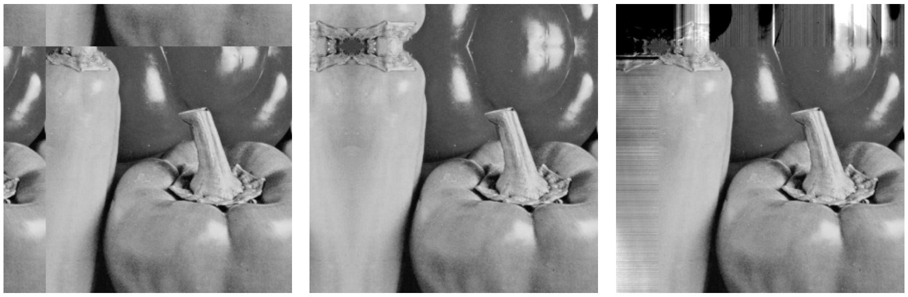

(a) Periodic BC (b) Reflective BC (c) Anti-reflective BC

Figure 1. Images that satisfy imposed boundary conditions. The original images of size 256 × 256 is extended across upper and left boundaries to 44 pixel rows and columns periodically (a), reflectively (b), and anti-reflectively (c).

of reflective and anti-reflective boundary condition methods, we shall apply CG iterations to the normal equation

$$(\mathbb{E}^*\mathcal{T}^*\mathcal{T}\mathbb{E} + \lambda\mathcal{I}_\Lambda)\,\mathbf{q} = \mathbb{E}^*\mathcal{T}^*\mathbf{g}, \tag{31}$$

derived from (4). We denote by RBC reflective boundary condition–based CG iterations, and we denote by ABC anti-reflective boundary condition–based CG iterations.

For explanatory purpose, we use the term *free boundary condition* to refer to the method suggested in [5, 6], even though the suggested method does not impose any boundary conditions whatsoever.

In [6], Calvetti et al. claim that, “In an Aristotelian approach to knowledge, when it is not known a priori which boundary conditions should be chosen, by admitting our lack of information it is possible to let the data itself determine them.” Thus, free boundary conditions do not need an extension operator to impose boundary conditions, and hence, this approach can be applied to arbitrarily shaped images. The proposed method in this paper will show that such flexibility in dealing with boundary artifacts gives several advantages to free boundary conditions over reflective and anti-reflective boundary conditions, which can be applied only to rectangular shaped images.

To test the performance of free boundary conditions, we shall apply the CG method to the linear system

$$(\mathcal{T}^*\mathcal{T} + \lambda\mathcal{I}_\Omega)\,\mathbf{p} = \mathcal{T}^*\mathbf{g}, \tag{32}$$

which is derived from the Tikhonov regularization (5). Form now on, we shall denote the standard CG iterations applied to (32) by FBC.

Before we close this section, it is worth to mention some research works related to direct deblurring methods. It is well known that that if the extension operator $\mathbb{E}$ in (31) is associated with periodic, reflective, or anti-reflective boundary conditions for symmetric PSFs (for a periodic boundary condition, the symmetry of PSF can be omitted), then the exact solution of (31) can be directly computable by using FFT for periodic boundary condition, discrete cosine transform (DCT) for reflective boundary condition, and discrete sine transform (DST) for anti-reflective boundary condition [12, 15, 3].

These fast transform based direct deblurring methods, however, usually present severe boundary artifacts. To reduce boundary artifacts, one can smooth the boundaries of the observed image to decay to 0 before those direct deblurring methods are applied to. This approach can reduce boundary artifacts in some degree, but, at the same time, makes it more difficult to recover near boundary image pixels. The method in [13] is designed to reduce this difficulty by extrapolating the observed image to smoothly decay to 0 in outside of Λ. Again, this approach can reduce boundary artifacts in some degree, but not sufficiently.

The performance of direct deblurring methods depends heavily on the feasibility of imposed boundary conditions. The difficulty of imposing *correct* boundary conditions is the main reason why iterative deblurring approaches to (31) have been considered, despite the fact that direct deblurring methods are available [15, 3, 7].

3. **Proposed method.**

3.1. **Free boundary condition.**

The use of the free boundary conditions begins with determining Ω from (22). We use Figure 2 to explain this process: Notice that the observed image $\mathbf{g}$ in Figure 2(a) has a non-rectangular boundary, where the dark background indicates the region where no observation is available. In Figure 2(a), the blurring is performed by 17×17 Gaussian PSF with standard deviation the width of 3 pixels. Figure 2(b) shows the pixel set Ω, which consists of two parts: one is the observed region Λ, indicated in white, and the unseen region $\Omega - \Lambda$, indicated in gray. Note that the border line between the white and the gray colored regions in Figure 2(b) is the boundary of the observed image $\mathbf{g}$. This process clearly shows that free boundary conditions can be applied to arbitrarily shaped images.

The free boundary condition alone, or equivalently FBC, does not remove boundary artifacts, as we can see in Figure 3(a), which is the deblurred image by FBC (the image is obtained by 100 CG iterations). Despite FBC failing to remove boundary artifacts, we suggest using FBC as the first step to avoid boundary artifacts caused by the use of inappropriate boundary conditions, by noting in the next section that boundary artifacts in FBC can be suppressed by using CG preconditioning.

3.2. **Preconditioned CG iterations.**

To deal with boundary artifacts, we propose a weight $\mathbf{w}$ defined by

$$\mathbf{w} = \mathcal{T}^* \mathbf{I}_\Lambda = \bar{\mathbf{k}} *_F \mathbf{I}_\Lambda, \tag{33}$$

on the domain Ω. The inner product defined by this weight as in (3) determines $L^2(\Omega, \mathbf{w})$. FBCW will denote CG iterations applied to the normal equation (9) derived from the $L^2(\Omega, \mathbf{w})$–based Tikhonov regularization (8).

Notice that the pixel value w_{j_1,j_2} of $\mathbf{w}$ represents the degree of the contribution of the image pixel at (j_1, j_2) to the observed image on Λ, through the blurring transform $\mathcal{T}$. For example, $w_{j_1,j_2} = 1$ (the maximum value w_{j_1,j_2} can have, by (19)) implies that the information at the image pixel (j_1, j_2) is spread out (by the blurring transform $\mathcal{T}$) to other image image pixels (i_1, i_2), all of which belong to Λ. In other words, none of the information at (j_1, j_2) is lost by the blurring. On the other hand, $0 < w_{j_1,j_2} < 1$ implies that $(1 - w_{j_1,j_2}) \times 100\%$ of information at the image pixel (j_1, j_2) is missing, or equivalently, not observed in the observed image on Λ, due to the truncation in observation.

The suggestion of the $\mathbf{w}$ based inner product in FBCW is motivated by the principle that the image pixel that gives less contribution to the observation should

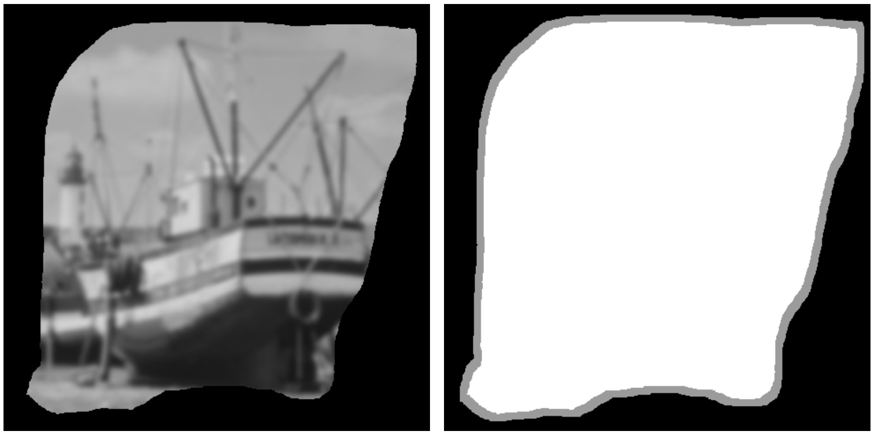

(a) Blurred image with a non-rectangular boundary

(b) Images pixels on Λ (white) and $\Omega - \Lambda$ (gray)

Figure 2. (a) A blurred image with a non-rectangular boundary. Here the blurring is generated by a 17×17 Gaussian PSF with standard deviation equal to the width of 3 pixels. The black background represents the region where no observation is available. (b) The set Ω of image pixels that can contribute to the observation through the 17×17 Gaussian PSF. The set Ω consists of two regions; observed image pixels, Λ, represented in white, and the unseen image pixels across the boundary, $\Omega - \Lambda$, represented in gray. The border line between white and gray colored regions is the boundary of the observed image.

be treated less importantly. FBCW, however, does not remove boundary artifacts. See Figures 16(b) and 17(b).

The failure of FBCW in removing boundary artifacts is expected, as the regularization parameter λ in FBCW must be set very small (in our simulation, $\lambda = 0.0001$), in order not to have over-smoothed results. In other words, the use of the **w**-based inner product in FBCW cannot be effective since λ is very small in FBCW. In fact, differences between the results of FBC and FBCW are hardly noticeable for any practical choice of λ.

To make the use of the **w**-based inner product effective, we consider the preconditioned CG iteration to (9) by a diagonal operator $\mathcal{W}$ defined by

$$(\mathcal{W}\mathbf{p})_{j_1,j_2} = w_{j_1,j_2} p_{j_1,j_2} \quad \text{for any image } \mathbf{p} \text{ defined on } \Omega. \tag{34}$$

Preconditioned conjugate gradient iterations of FBCW are equivalent to standard conjugate gradient iterations applied to

$$[\mathcal{W}^{-1/2}\,(\mathcal{T}^*\mathcal{T} + \lambda\mathcal{W})\,\mathcal{W}^{-1/2}](\mathcal{W}^{1/2}\mathbf{p}) = \mathcal{W}^{-1/2}\mathcal{T}^*\mathbf{g}, . \tag{11$'$}$$

We shall denote by FBCWP conjugate gradient iterations applied to (11).

Figure 3(b) shows the deblurred image by FBCWP (the image is obtained by 100 CG iterations). The boundary artifacts in Figure 3(a) are completely removed in Figure 3(b).

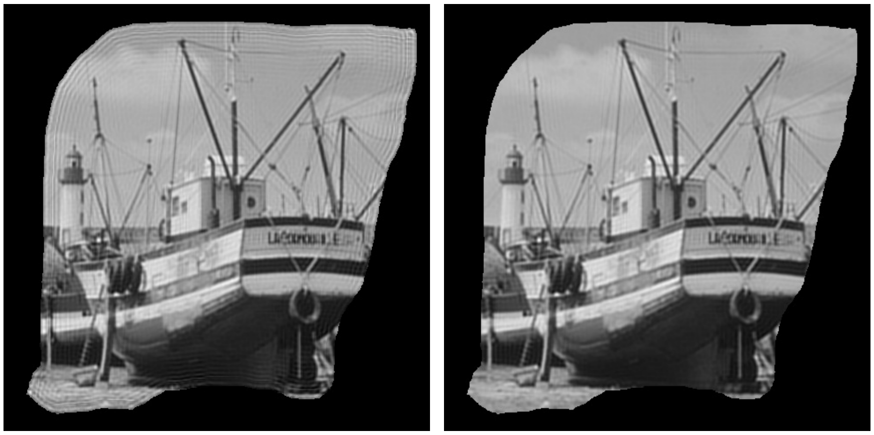

(a) FBC

(b) FBCWP

FIGURE 3. (a) The deblurred image by FBC from Figure 2(a). Those ripples are propagating into the center area as the iteration proceeds. (b) The deblurred image by FBCWP from Figure 2(a). The deblurred image shows no boundary artifacts at all. This result shows that FBCWP can deblur arbitrarily shaped images, without causing boundary artifacts.

To make clear, the exact solutions of the two linear systems

$$\mathcal{W}^{-1/2}\left(\mathcal{T}^*\mathcal{T}+\lambda\mathcal{W}\right)\mathcal{W}^{-1/2}\mathcal{W}^{1/2}\mathbf{p}=\mathcal{W}^{-1/2}\mathcal{T}^*\mathbf{g}$$

and

$$\left(\mathcal{T}^*\mathcal{T}+\lambda\mathcal{W}\right)\mathbf{p}=\mathcal{T}^*\mathbf{g}$$

are the *same*; nonetheless, the sequence of conjugate-gradient iterates for both linear systems generally *differ* until they converge to the exact solution (assuming exact arithmetic) at the final, $\dim(L^2(\Omega))$th, iterate. Because the best results are obtained after a relatively small number of iterates, our result images differ.

4. **Simulation results.** We conducted simulation studies to compare incomplete CG iterations applied to the following normal equations in boundary artifact removal in image deblurring:

- **RBC**: Reflective boundary conditions and incomplete CG iteration applied to

$$\left(\mathbb{E}^*\mathcal{T}^*\mathcal{T}\mathbb{E}+\lambda\mathcal{I}_\Lambda\right)\mathbf{q}=\mathbb{E}^*\mathcal{T}^*\mathbf{g}, \tag{31'}$$

  where $\mathbb{E}$ is the extension operator associated with the reflective boundary condition.
- **ABC**: Anti-reflective boundary conditions and incomplete CG iteration applied to (31) with the extension operator $\mathbb{E}$ that is associated with the anti-reflective boundary condition.
- **FBC**: Free boundary conditions and incomplete CG iteration applied to

$$\left(\mathcal{T}^*\mathcal{T}+\lambda\mathcal{I}_\Omega\right)\mathbf{p}=\mathcal{T}^*\mathbf{g}. \tag{32'}$$

- **FBCW**: Free boundary conditions, $L^2(\Omega, \mathbf{w})$–weighted norm, and incomplete CG iteration applied to

$$(\mathcal{T}^*\mathcal{T} + \lambda\mathcal{W})\,\mathbf{p} = \mathcal{T}^*\mathbf{g}. \tag{9'}$$

- **FBCWP**: Free boundary conditions, $L^2(\Omega, \mathbf{w})$–weighted norm, and incomplete CG iteration applied to

$$[\mathcal{W}^{-1/2}\,(\mathcal{T}^*\mathcal{T} + \lambda\mathcal{W})\,\mathcal{W}^{-1/2}](\mathcal{W}^{1/2}\mathbf{p}) = \mathcal{W}^{-1/2}\mathcal{T}^*\mathbf{g}. \tag{11'}$$

- **FBCP**: Free boundary conditions and incomplete CG iteration applied to

$$[\mathcal{W}^{-1/2}\,(\mathcal{T}^*\mathcal{T} + \lambda\mathcal{I}_\Omega)\,\mathcal{W}^{-1/2}](\mathcal{W}^{1/2}\mathbf{p}) = \mathcal{W}^{-1/2}\mathcal{T}^*\mathbf{g}. \tag{35}$$

In most case, we shall omit results by FBCW and FBCP, since they are almost identical to results by FBC and FBCWP, respectively. Here we note that the “incomplete CG iteration” is a necessary requirement to avoid noise amplification that would be generated by “complete CG iteration”.

In simulation studies, we used the “Airfield” image in Figure 4(a), as the true image $\mathbf{f}$, and three different PSFs (uniform, Gaussian, and diagonal gradient) as our image blurring models.

For noise model, we used a noise $\mathbf{n}$ such that such as

$$\mathbf{n} \sim \text{Normal}(\mathbf{0}, \sigma^2 \mathrm{I}_{|\Lambda|}), \tag{36}$$

where $\mathbf{0}$ is the all zero image defined on Λ and $\mathrm{I}_{|\Lambda|}$ is the $|\Lambda| \times |\Lambda|$ identity matrix. Throughout his paper, we assume that the standard deviation σ in (36) is set to be 0.5% of the average value of $\mathcal{T}\mathbf{f}$. We use such little noise so that changes in boundary artifacts will be visually noticeable.

We chose the deblurred image that had the smallest RSE (Relative Square Error) in 200 iterations for each simulation. Here the RSE is defined by

$$\text{RSE} = \frac{\sum_{i_1,i_2} |\tilde{f}_{i_1,i_2} - f_{i_1,i_2}|^2}{\sum_{i_1,i_2} |f_{i_1,i_2}|^2}, \tag{37}$$

where $\tilde{f}_{i_1,i_2}$ and f_{i_1,i_2} are pixel values of the deblurred image and the true image, respectively, at the pixel $(i_1, i_2) \in \Lambda$. This restriction is made for fair comparison. Notice that RBC and ABC recover images that are the same size as the observed image, while FBC, FBCW, and FBCWP recover images with all pixels that give any contributions to the observed image. For instance, in the simulation with the 11×11 uniform PSF and the true image of size 500×500, the size of deblurred images by FBC, FBCW, and FBCWP is 500×500, while the size of deblurred images by RBC and ABC is 490×490. For fair visual comparison, however, our figures present image results from FBC, FBCW, and FBCWP after removing unseen image pixels.

4.1. Summary of claims and supporting figures.

In this section we give a list of our claims with the figures that support them.

- The proposed method FBCWP removes boundary artifacts better than the other methods (RBC, ABC, FBC) when images are blurred with a uniform point spread function. Figures 5 and 6 support this claim.
- While FBCWP removes boundary artifacts better than the other methods when images are blurred with a Gaussian point spread function, the differences, while noticeable, are not as large as with uniform blurring. Figures 8 and 9 support this claim.

- Figures 11 and 12 show that FBCWP works significantly better than the other methods when the point spread function is a one-dimensional diagonal gradient blur.
- Boundary artifacts can occur even when there are no "unseen" pixels across the boundary (pixels on $\Omega - \Lambda$). The bottom and right boundaries of the images in Figures 11 and 12, which are blurred with a diagonal gradient point spread function, illustrate this claim.
- Our proposed method FBCWP removes boundary artifacts better than the other methods over a wide range of regularization parameters λ. Figures 5, 13, 14, and 15 illustrate the truth of this claim for uniform blurring.
- Preconditioning by $\mathcal{W}$ is essential. Even though the use of the weighted norm $L^2(\Omega, \mathbf{w})$ alone is not enough to achieve good boundary artifact removal, combined with preconditioning by $\mathcal{W}$, it extends boundary artifact removal effect by the preconditioner $\mathcal{W}$ to unseen image pixels. Figures 16 and 17 support this claim.
- Our FBCWP method recovers certain blurred, damaged images better than previous methods that use median filtering to recover missing data pixels before deblurring. Figures 18 and 19 illustrate this point.
- The FBCWP method can recover blurred images with salt-and-pepper noise. This is shown in Figures 20 and 21.

The following sections discuss these claims in more detail.

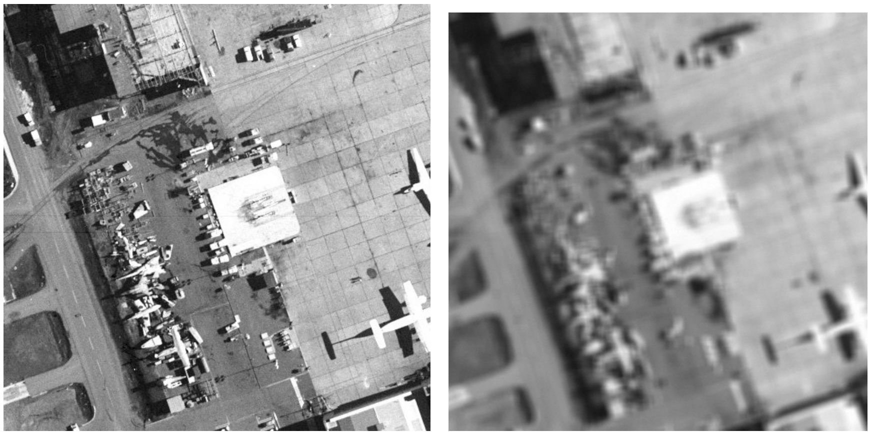

(a) True image

(b) Blurred by uniform PSF

FIGURE 4. (a) The true "Airfield" image $\mathbf{f}$ of size 500×500. (b) The observed image $\mathbf{g} = \mathcal{T}\mathbf{f} + \mathbf{n}$, where $\mathcal{T}$ is defined by the 11×11 uniform PSF $\mathbf{k}$ as in (2) and $\mathbf{n}$ is Gaussian noise defined in (36). The size of $\mathbf{g}$ is of 490×490 pixels.

4.2. **Reduction of boundary artifacts.** In this simulation, we used $\lambda = 0.001$ as the regularization parameter for all PSFs. We will discuss simulation results with other regularization parameters in Section 4.3.

4.2.1. *Uniform blurring.* Figure 4(b) shows a noisy blurred image $\mathbf{g} = \mathcal{T}\mathbf{f} + \mathbf{n}$, where $\mathcal{T}$ is the blurring transform defined by the 11×11 uniform PSF, $\mathbf{f}$ is the true

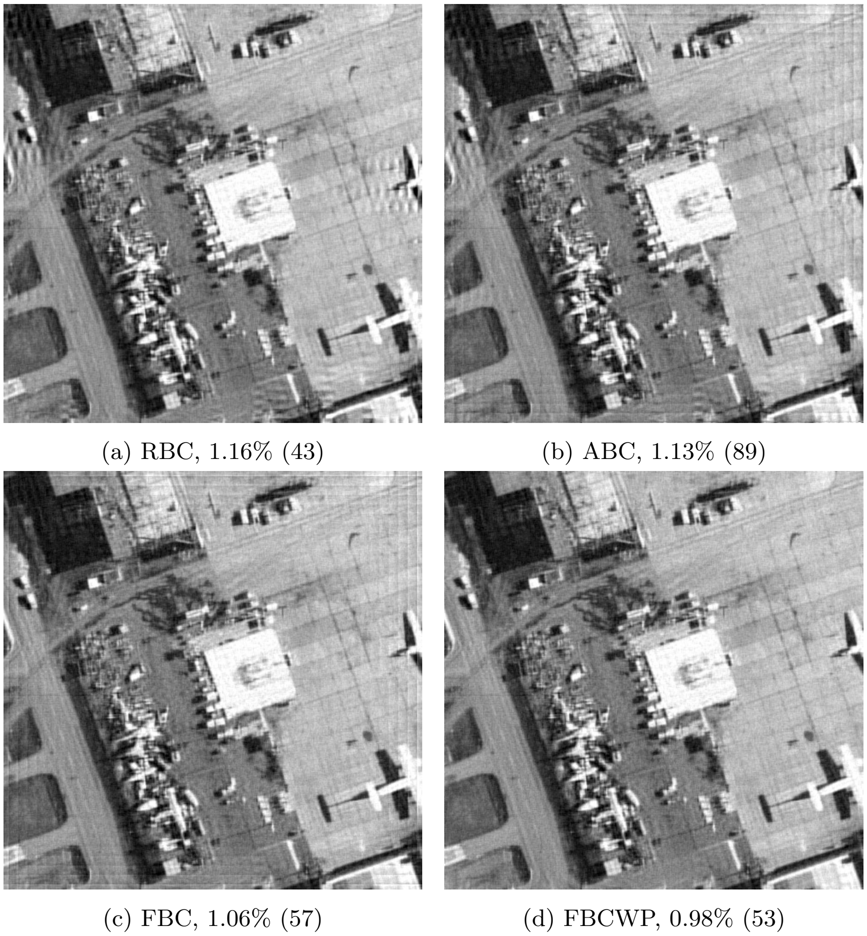

(a) RBC, 1.16% (43)

(b) ABC, 1.13% (89)

(c) FBC, 1.06% (57)

(d) FBCWP, 0.98% (53)

Figure 5. Deblurred images by RBC (a), ABC (b), FBC (c), and FBCWP (d) from Figure 4(b), which is blurred by 11 × 11 uniform PSF. For each method, the smallest RSE is shown with the corresponding iteration number inside the parenthesis. All images are of size 490 × 490. RBC (a) suffered from boundary artifacts in the region where the reflected boundary did not provide a sufficient similarity in image pixels across the boundary. ABC (b) and FBC (c) suffered from boundary artifacts at all regions near boundary. FBCWP (d) did not show any noticeable boundary artifacts.

image in Figure 4(a), and $\mathbf{n}$ is the Gaussian noise in (36). Figure 5 shows deblurred images by RBC, ABC, FBC, and FBCWP, using the image in Figure 4(b) as input. In this simulation, RBC, ABC, FBC, and FBCWP attain their RSE minimums, 1.16%(43), 1.13%(89), 1.06%(57), and 0.98%(53), respectively. Here the number in the parenthesis is the iteration number that attains the smallest RSE for each method.

Figure 5 shows that all methods (RBC, ABC, FBC, and FBCWP) produce almost identical results in the center part in deblurred images, but they are very different in boundary artifact removal. The boundary artifacts in RBC (Figure 5(a)) are less

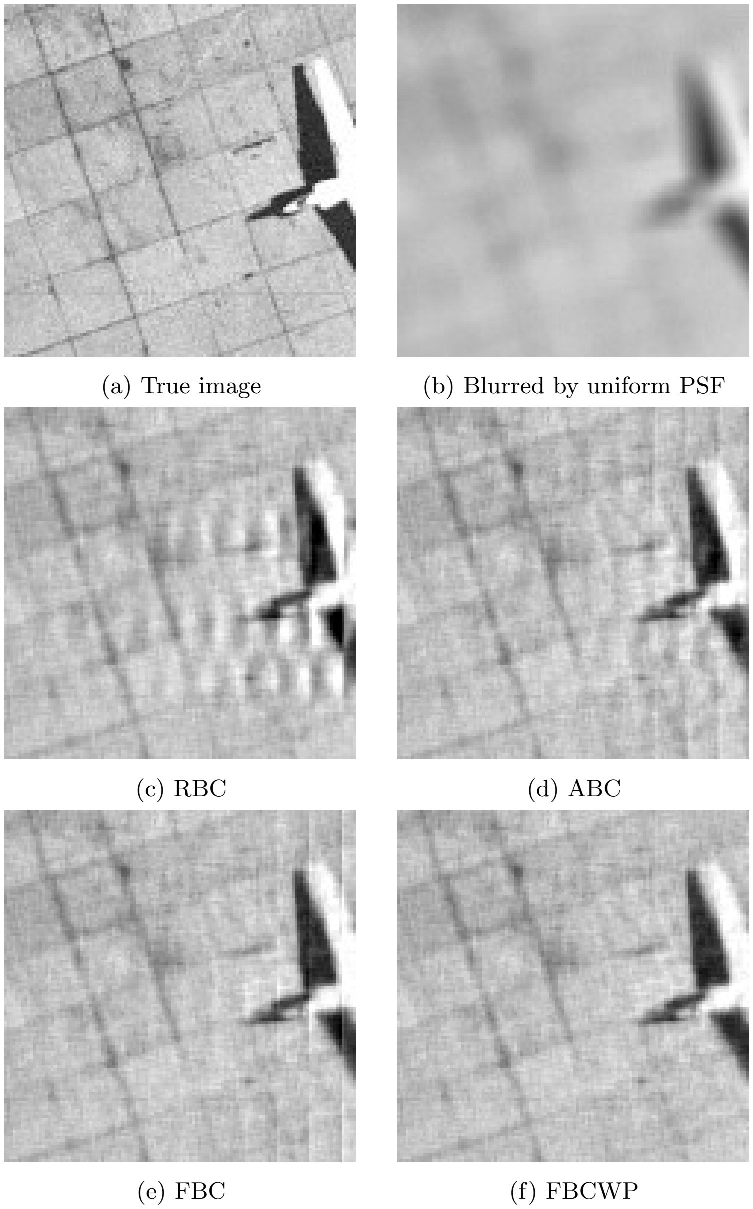
(a) True image

(b) Blurred by uniform PSF

(c) RBC

(d) ABC

(e) FBC

(f) FBCWP

Figure 6. The zoomed parts of the "Airfield" images. All images are of size 120 × 120. In deblurred images by RBC, ABC, and FBC, propagating boundary artifacts appear, while no boundary artifacts appear in FBCWP. (a) A part of the true image in Figure 4(a). (b) A part of the observed image in Figure 4(b). (c) A part of the deblurred image by RBC in Figure 5(a). (d) A part of the deblurred image by ABC in Figure 5(b). (e) A part of the deblurred image by FBC in Figure 5(c). (f) A part of the deblurred image by FBCWP in Figure 5(d).

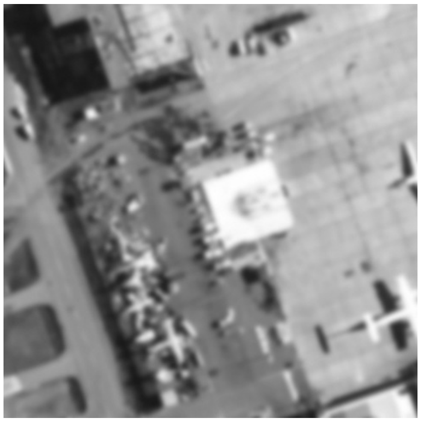

FIGURE 7. The observed image $\mathbf{g}$, which is blurred by a 17×17 Gaussian PSF with standard deviation equal to the width of 3 pixels and corrupted by Gaussian noise $\mathbf{n}$ defined in (36). The size of the observed image $\mathbf{g}$ is of 484×484.

annoying than those in ABC (Figure 5(b)); they appear only in some parts, while the boundary artifacts in ABC appear all over image pixels near boundaries. A similar phenomenon also holds for FBC (Figure 5(c)). On the other hand, FBCWP does not show any noticeable boundary artifacts. See zoomed images in Figure 6 for detailed comparison.

In our simulation, the trends described in this section also held for other test images; FBCWP outperformed RBC, ABC, and FBC objectively, by having smaller RSE than RBC, ABC, and FBC, and subjectively, by not showing boundary artifacts for all test images.

4.2.2. *Gaussian blurring.* Figure 7 shows a noisy blurred image $\mathbf{g}$, where the blurring is computed by a 17×17 Gaussian PSF with standard deviation equal to the width of 3 pixels.

Figure 8 shows deblurred images by RBC, ABC, FBC, and FBCWP, from the image in Figure 6. In this simulation, RBC, ABC, FBC, and FBCWP attain their RSE minimums, 1.29%(82), 1.49%(99), 1.29%(90), and 1.22%(77), respectively. Here the number in the parenthesis is, again, the iteration number that attains the smallest RSE for each method.

In this simulation, all methods produce almost identical results in the center part in deblurred images, and they show some difference in boundary artifact removal. Again, FBCWP does not show any noticeable boundary artifacts, while RBC, ABC, and FBC show mild boundary artifacts. Unlike the simulation with the uniform blurring, however, the boundary artifacts in RBC, ABC, and FBC do not propagate into center parts of deblurred images. Zoomed images in Figure 9 show detailed comparison.

In our simulation, the trends described in this section also held for other test images; RBC, ABC, and FBC do not severely suffer from boundary artifacts under Gaussian blurring in the sense that those non-propagating boundary artifacts can easily be removed by cropping out a few rows and columns of image pixels near the boundary, while FBCWP does not show any sign of boundary artifacts.

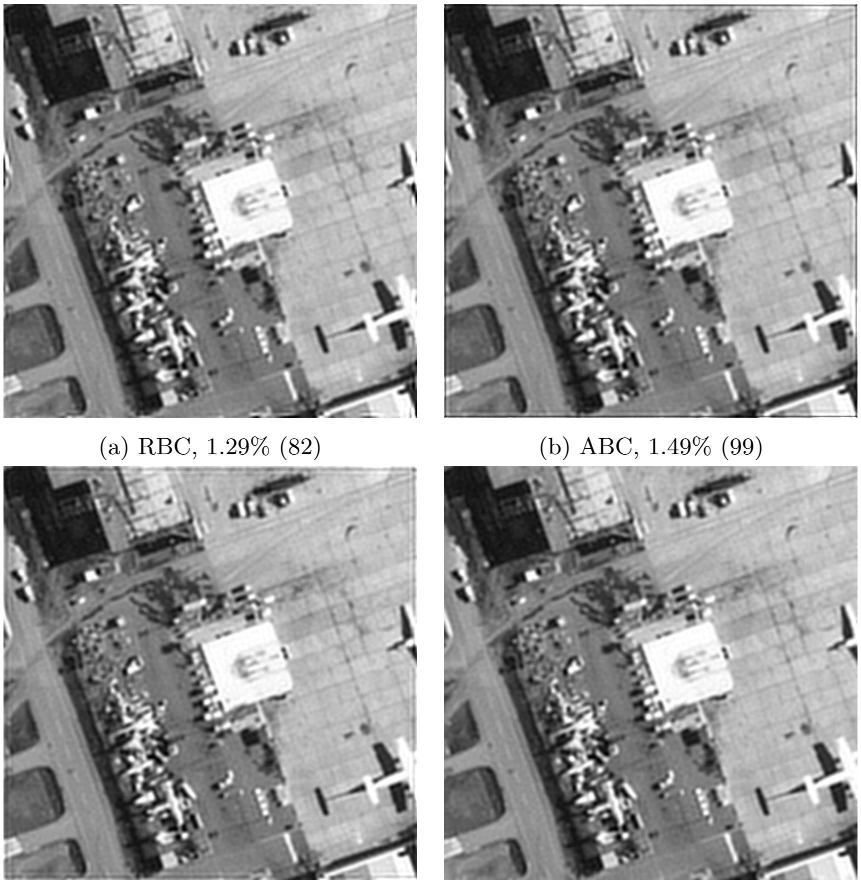

(a) RBC, 1.29% (82)

(b) ABC, 1.49% (99)

(c) FBC, 1.29% (90)

(d) FBCWP, 1.22% (77)

Figure 8. Deblurred images by RBC (a), ABC (b), FBC (c), and FBCWP (d) from Figure 7, which is blurred by 11 × 17 Gaussian PSF. For each method, the smallest RSE is shown with the corresponding iteration number inside the parenthesis. All images are of size 484 × 484. RBC (a) generated mild non-propagating boundary artifacts in the region where the reflected boundary was not similar to the true image pixels across the boundary. ABC (b) and FBC (c) generated mild non-propagating boundary artifacts in all regions near boundary. FBCWP (d) did not show boundary artifacts.

We speculate that boundary artifacts do not propagate to the interior of the image when using RBC and ABC in this example because of some special property of Gaussian blurring, perhaps because the Gaussian PSF we use decays quickly away from its center. We also note that FBC does not propagate boundary artifacts under Gaussian blurring, even though it does not impose any boundary conditions.

4.2.3. *Diagonal gradient blurring.* Figure 10 shows a noisy blurred image $\mathbf{g} = \mathcal{T}\mathbf{f} + \mathbf{n}$, where the blurring transform $\mathcal{T}$ is computed by the 11 × 11 diagonal gradient

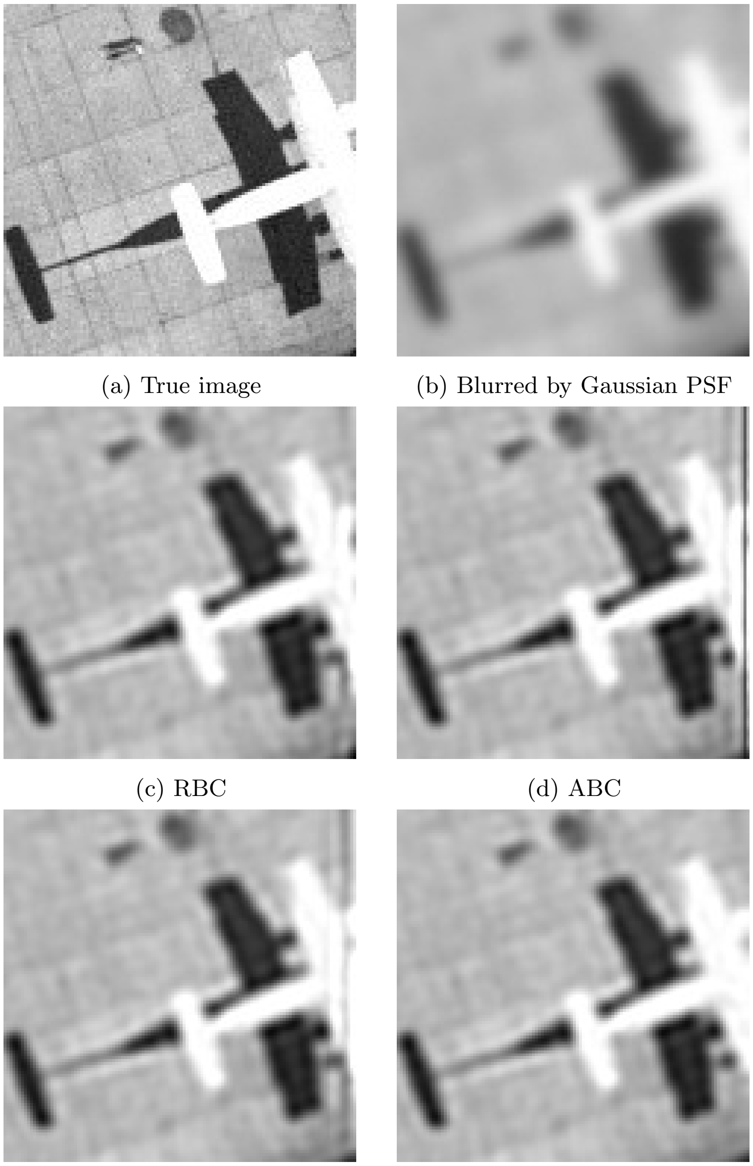

(a) True image

(b) Blurred by Gaussian PSF

(c) RBC

(d) ABC

(e) FBC

(f) FBCWP

Figure 9. The zoomed parts of the "Airfield" images. All images are of size 120 × 120. In deblurred images by RBC, ABC, and FBC, non-propagating boundary artifacts appear, while no boundary artifacts appear in FBCWP. (a) A part of the true image in Figure 4(a). (b) A part of the observed image in Figure 7. (c) A part of the deblurred image by RBC in Figure 8(a). (d) A part of the deblurred image by ABC in Figure 8(b). (e) A part of the deblurred image by FBC in Figure 8(c). (f) A part of the deblurred image by FBCWP in Figure 8(d).

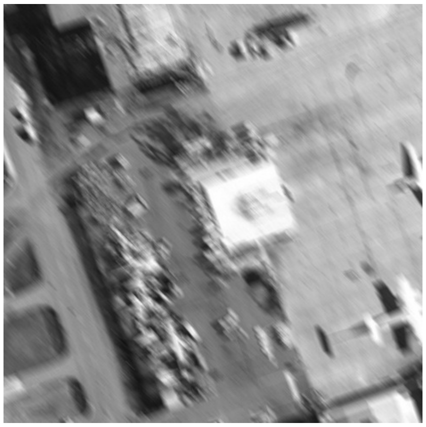

Figure 10. The observed image $\mathbf{g} = \mathcal{T}\mathbf{f} + \mathbf{n}$, where $\mathcal{T}$ is defined by an 11×11 diagonal gradient PSF with diagonal elements $\{\frac{30}{275}, \frac{29}{275}, \ldots, \frac{20}{275}\}$ as in (2), where the first diagonal element $\frac{30}{275}$ is $k_{0,0}$, and $\mathbf{n}$ is Gaussian noise defined in (36). The size of the observed image $\mathbf{g}$ is of 490×490.

PSF represented by a matrix whose main diagonal elements are $\{\frac{30}{275}, \frac{29}{275}, \ldots, \frac{20}{275}\}$, where the first diagonal element $\frac{30}{275}$ is $k_{0,0}$.

Figure 11 shows deblurred images by RBC, ABC, FBC, and FBCWP, from the image in Figure 10. In this simulation, RBC, ABC, FBC, and FBCWP attain their RSE minimums, 0.78%(20), 0.46%(155), 0.45%(38), and 0.31%(34), respectively. Here the number in parentheses is, again, the iteration number that attains the smallest RSE for each method.

RBC (Figure 11(a)) shows boundary artifacts in some regions near the left boundary and at the whole region along the lower and right boundaries. Boundary artifacts near the lower and right boundaries in Figure 11(a) form straight lines that are parallel to the boundary line. Similar pattern are also shown near the lower and right boundaries in ABC (Figure 11(b)) and FBC (Figure 11(c)), but they are not as severe as those in RBC (Figure 11(a)). On the other hand, FBCWP does not show any sign of boundary artifacts. Zoomed images in Figure 12 show detailed comparison.

The assumption that the first diagonal element of $\mathbf{k}$ is $k_{0,0}$ indicates that $\Omega = \{(j_1, j_2) \mid -10 \le j_\nu < 490,\ \nu = 1, 2\}$ and $\Lambda = \{(i_1, i_2) \mid 0 \le i_\nu < 490,\ \nu = 1, 2\}$, and hence there are no unseen image pixels across the lower and right boundaries in Figure 10, while ten rows and ten columns of image pixels are across the upper and left boundaries, respectively. Based on this observation, one might expect that RBC, ABC, and FBC would not suffer from artifacts near the lower and right boundaries, since there are no unseen image pixels across the lower and right boundaries. The simulation results in this section, however, clearly show that such an expectation would be wrong. In other words, the existence of unseen image pixels is not the source of boundary artifacts.

Again, the trends described in this section held for other test images in our simulation. In all test images, RBC, ABC, and FBC suffered from propagating boundary artifacts, while FBCWP showed no sign of boundary artifacts. Moreover, in all test images, FBCWP outperformed RBC, ABC, and FBC in the RSE criterion.

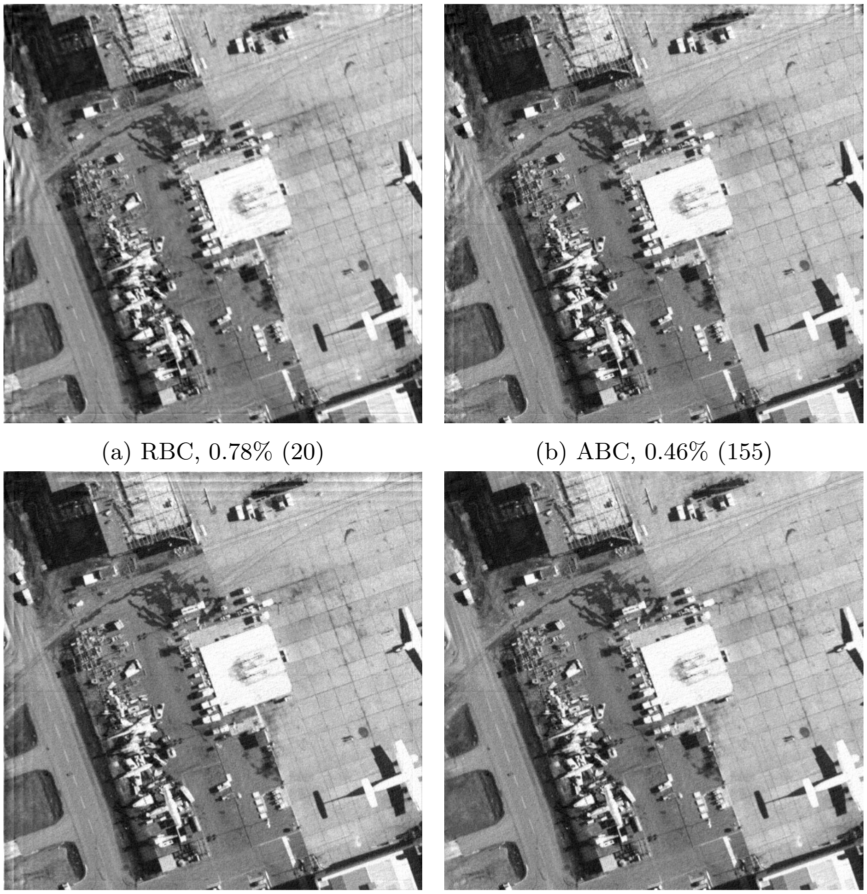

(a) RBC, 0.78% (20)

(b) ABC, 0.46% (155)

(c) FBC, 0.45% (38)

(d) FBCWP, 0.31% (34)

Figure 11. Deblurred images by RBC (a), ABC (b), FBC (c), and FBCWP (d) from Figure 10, which is blurred by 11 × 11 diagonal gradient PSF. For each method, the smallest RSE is shown with the corresponding iteration number inside the parenthesis. All images are of size 490 × 490. RBC (a) generated propagating boundary artifacts at some part near the left boundary an propagating boundary artifacts in all regions near the lower and right boundaries. ABC (b) generated propagating boundary artifacts at some part near the left boundary and propagating boundary artifacts in all regions near the lower and right boundaries, as RBC did. The severity of boundary artifacts in ABC is weaker than that of RBC, however. FBC (c) generated propagating boundary artifacts in all regions near all boundaries. Boundary artifacts near the upper and left boundaries look more severe than those near the lower and right boundaries. FBCWP (d) did not show boundary artifacts.

4.3. **Selection of regularization parameter.** The simulation results in Section 4.2 showed that, when the fixed regularization parameter $\lambda = 0.001$ was used,

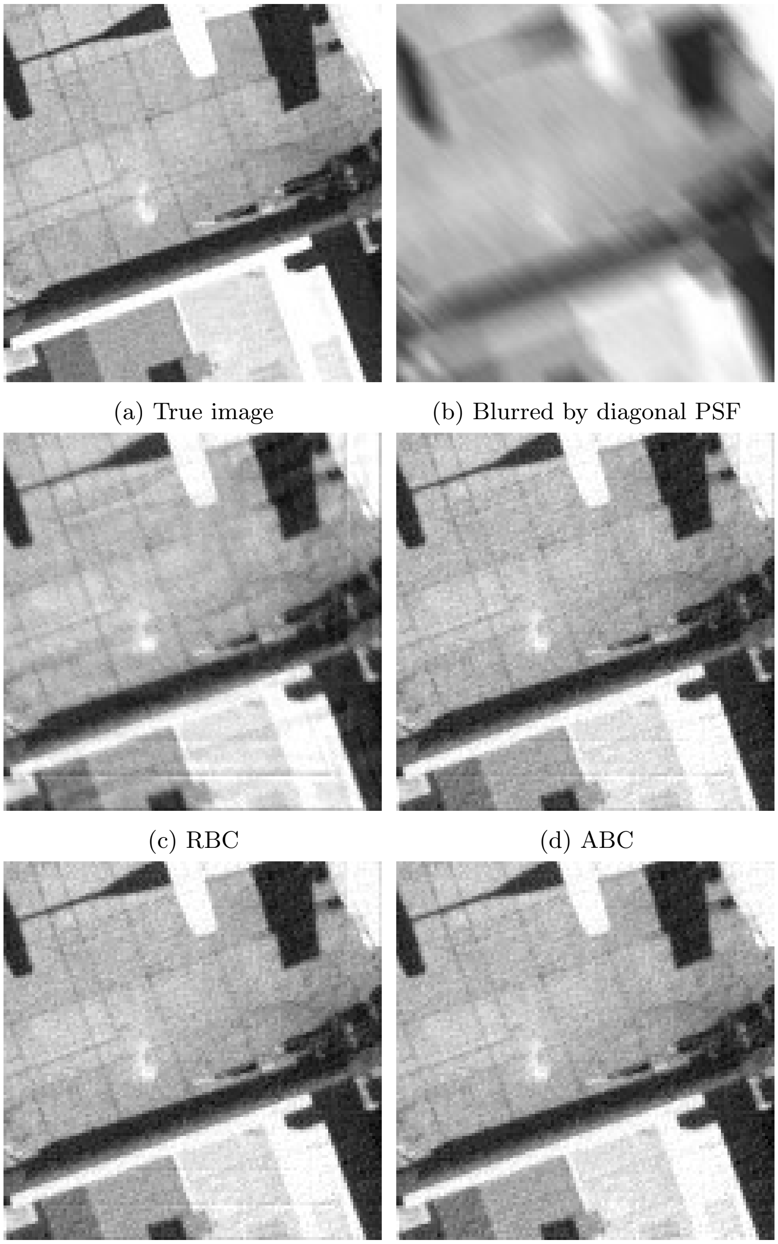

(a) True image

(b) Blurred by diagonal PSF

(c) RBC

(d) ABC

(e) FBC

(f) FBCWP

Figure 12. Figure 12. The zoomed parts of 'Airfield' images. All images are of size 120 × 120. (a) A part of the true image in Figure 4(a). (b) A part of the observed image in Figure 10. (c) A part of the deblurred image by RBC in Figure 11(a). (d) A part of the deblurred image by ABC in Figure 11(b). (e) A part of the deblurred image by FBC in Figure 11(c). (f) A part of the deblurred image by FBCWP in Figure 11(d).

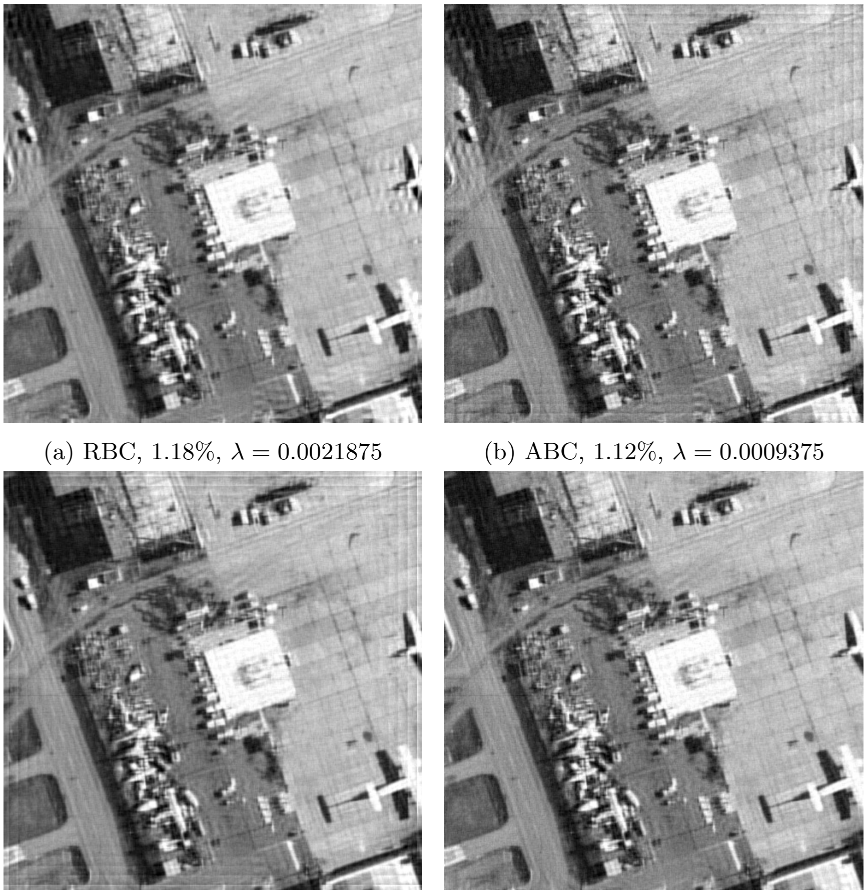

(a) RBC, 1.18%, $\lambda = 0.0021875$

(b) ABC, 1.12%, $\lambda = 0.0009375$

(c) FBC, 1.16%, $\lambda = 0.0021875$

(d) FBCWP, 1.02%, $\lambda = 0.0015625$

Figure 13. Deblurred images by RBC (a), ABC (b), FBC (c), and FBCWP (d) with near-optimal regularization parameters from Figure 4(b), which is blurred by 11×11 uniform PSF and corrupted by the Gaussian noise $\mathbf{n}$ in (36). Here near-optimal regularization parameters were computed by the fifth approximates of the bisection method starting from 0.0 and 0.01. For each method, the RSE at the 100-th iteration was written. Results showed that RBC (a), ABC (b), and FBC (c) exhibited boundary artifacts with near-optimal regularization parameters, while FBCWP (d) did not.

FBCWP outperformed RBC, ABC, and FBC in deblurring of uniform, Gaussian, and diagonal gradient PSFs in the presence of Gaussian noise $\mathbf{n}$. In the previous section, we used $\lambda = 0.001$ as the single regularization parameter for all methods (RBC, ABC, FBC, and FBCWP), despite the difference in PSFs, test images, and methods, by noting that $\lambda = 0.001$ produced the smallest RSE result among various λ's (0.1, 0.01, 0.001, 0.0001, 0.00001, 0.0) for RBC, ABC, FBC, and FBCWP, in the simulation with the true image, "Airfield"(Figure 4(a)), the 11×11 uniform PSF, and the Gaussian noise $\mathbf{n}$ in (36). Since the optimal regularization parameter depends on the true image $\mathbf{f}$, the PSF $\mathbf{k}$, the method, and the noise $\mathbf{n}$, one might

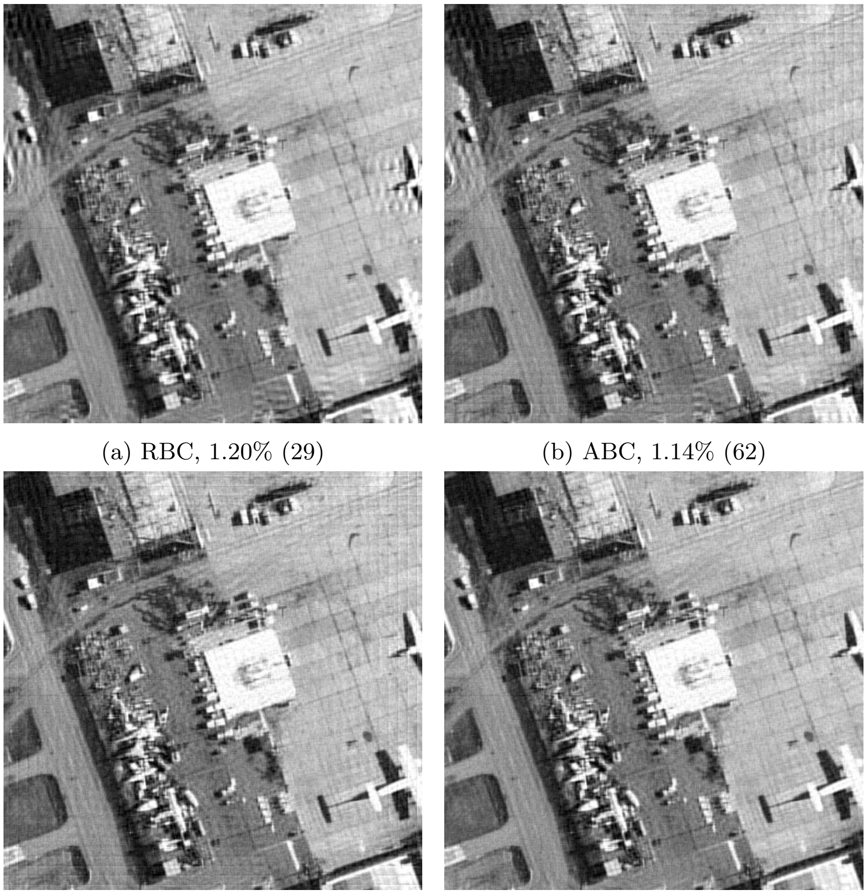

(a) RBC, 1.20% (29)

(b) ABC, 1.14% (62)

(c) FBC, 1.08% (39)

(d) FBCWP, 0.99% (35)

Figure 14. Deblurred images by RBC (a), ABC (b), FBC (c), and FBCWP (d) with $\lambda = 0.0$ as the regularization parameter from Figure 4(b), which is blurred by 11×11 uniform PSF and corrupted by the Gaussian noise $\mathbf{n}$ in (36). For each method, the smallest RSE is shown with the corresponding iteration number inside the parenthesis. Results showed that RBC (a), ABC (b), and FBC (c) exhibited boundary artifacts with no Tikhonov regularization (i.e., $\lambda = 0.0$), while FBCWP (d) did not.

suspect that different λ's would give a chance for RBC, ABC, or FBC to outperform FBCWP. The simulation results, however, show that this does not happen.

In our simulation studies, for any reasonable choice for the regularization parameter λ, FBCWP outperformed RBC, ABC, and FBC without exceptions in test images or blurring PSFs, by having the smallest RSE and not showing any sign of boundary artifacts. Moreover, the regularization parameter λ did not give noticeable differences in RBC, ABC, FBC, and FBCWP. These are well expected results, since RBC, ABC, FBC, and FBCWP are virtually identical CG iterations; the only differences are made on ways of treating image pixels near boundaries. Based on this argument, we can conclude that the superior performance of FBCWP over

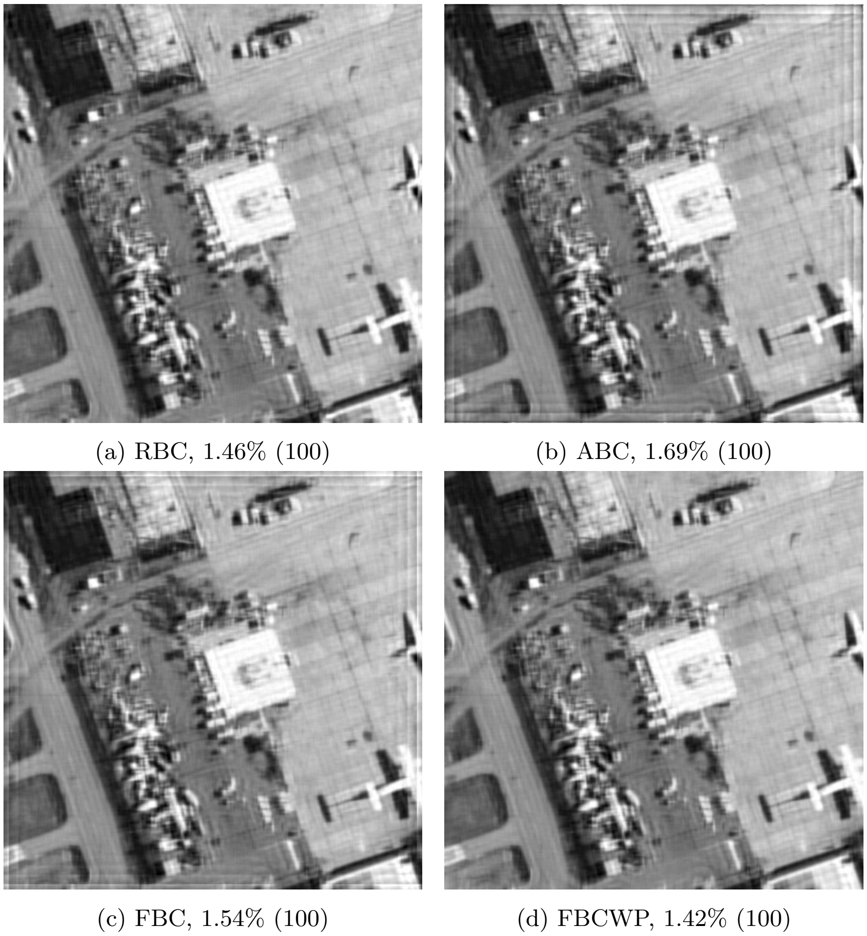

(a) RBC, 1.46% (100)

(b) ABC, 1.69% (100)

(c) FBC, 1.54% (100)

(d) FBCWP, 1.42% (100)

Figure 15. Deblurred images by RBC (a), ABC (b), FBC (c), and FBCWP (d) with $\lambda = 0.01$ as the regularization parameter from Figure 4b, which is blurred by 11×11 uniform PSF and corrupted by the Gaussian noise $\mathbf{n}$ in (36). For each method, the RSE at the 100-th iteration was shown. Results showed that RBC (a), ABC (b), and FBC (c) exhibited boundary artifacts with $\lambda = 0.01$ as the regularization parameter, while FBCWP (d) did not.

RBC, ABC, and FBC, which was shown in simulations with $\lambda = 0.001$ as the regularization parameter, also holds for any other reasonable regularization parameters.

To support this claim, we present Figures 13, 14, and 15 to show improved suppression of boundary artifacts by FBCWP over RBC, ABC, and FBC in a wide range of regularization parameters. Figures 13, 14, and 15 show deblurred images with near-optimal regularization parameters, $\lambda = 0.0$ as an example of under-estimated regularization parameters, and $\lambda = 0.01$ as an example of over-estimated regularization parameters, respectively. Results in Figures 13, 14, and 15 show that any reasonable choices for regularization parameters or iteration numbers do not give significant impact on boundary artifact removal; RBC, ABC, and FBC

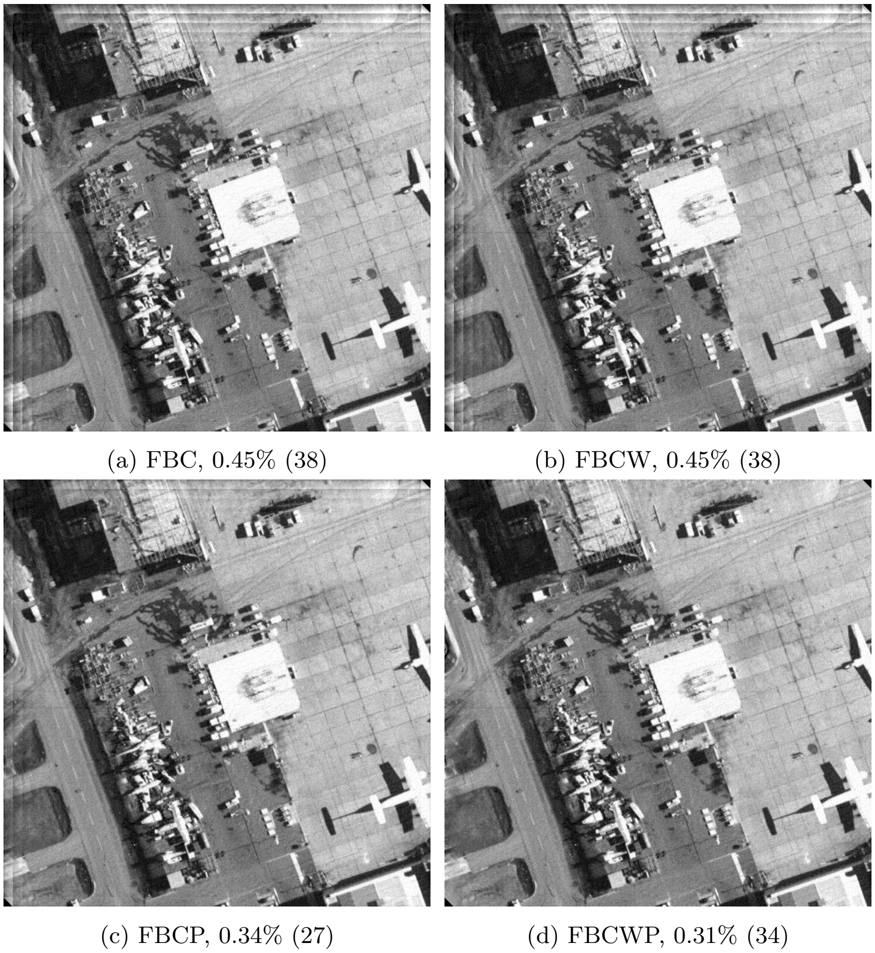

(a) FBC, 0.45% (38)

(b) FBCW, 0.45% (38)

(c) FBCP, 0.34% (27)

(d) FBCWP, 0.31% (34)

Figure 16. Deblurred images by FBC (a), FBCW (b), FBCP (c), and FBCWP (d) from the image in Figure 10, which is blurred by 11×11 diagonal gradient PSF and corrupted by the Gaussian noise $\mathbf{n}$ in (36). For each method, the smallest RSE is shown with the corresponding iteration number inside the parenthesis. Here deblurred images on Ω, not on Λ, are shown (in this paper, only Figures 16 and 17 show recovered pixels on $\Omega - \Lambda$). Thus, images in this figure are of size 500×500. The comparison of FBCP (c) with FBC (a) and that of FBCWP (d) with FBCW (b) show that the use of the preconditioner $\mathcal{W}$ removes boundary artifacts. Even though the difference is not very noticeable, the comparison of FBCWP (d) with FBCP (c) shows some improvement made by the use of the regularization by $L^2(\Omega, \mathbf{w})$ in recovering image pixels on $\Omega - \Lambda$.

suffers from boundary artifacts for any reasonable pairs of regularization parameters and iteration numbers, while FBCWP does not.

By noticing the effective suppression of boundary artifacts by FBCWP, we can easily estimate regularization parameters for FBCWP by considering the special

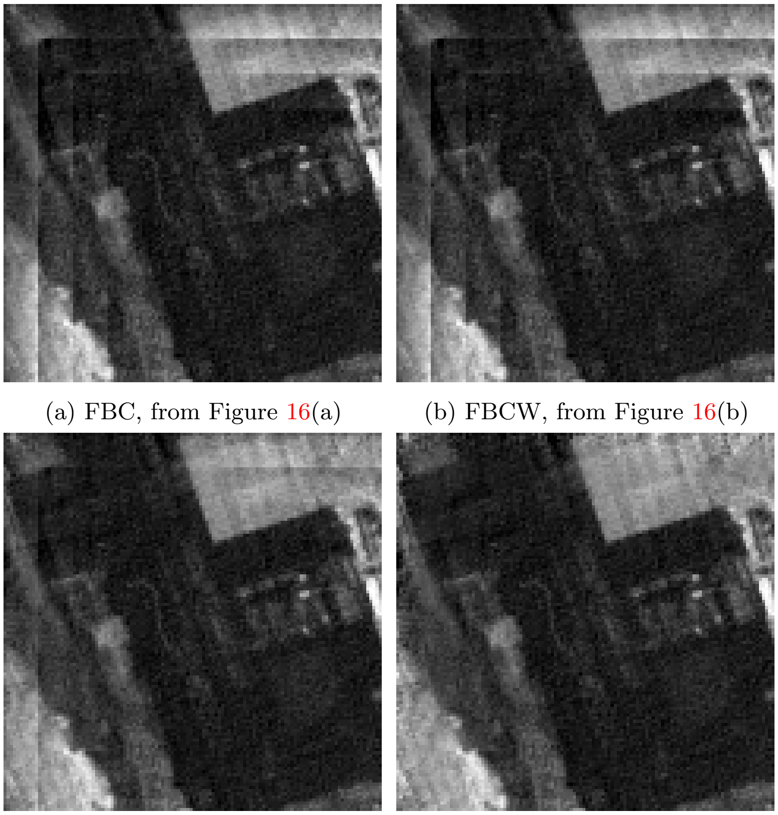

(a) FBC, from Figure 16(a) (b) FBCW, from Figure 16(b)

(c) FBCP, from Figure 16(c) (d) FBCWP, from Figure 16(d)

Figure 17. The zoomed parts of 'Airfield' images in Figure 16. All images are of size 120 × 120. Images in this figure show that FBCWP (d) removes boundary artifacts not only in Λ but also in $\Omega - \Lambda$, while FBCP (c) suffers from boundary artifacts in $\Omega - \Lambda$, and FBC (a) and FBCW (b) suffer from boundary artifacts not only in $\Omega - \Lambda$, but also in near boundary pixels in Λ.

cases at which the true image $\mathbf{f}$ in image deblurring problem $\mathbf{g} = \mathcal{T}\mathbf{f} + \mathbf{n}$ (1) satisfy periodic boundary conditions. In such cases the blurring transform $\mathcal{T}$ can be regarded as a circular convolution and the preconditioner $\mathcal{W}$ becomes the identity matrix $\mathcal{I}_\Lambda$. Moreover, the resulting image $\mathbf{p}$ of complete CG iterations of FBCWP can be directly computable by

$$\mathbf{p} = \mathrm{IFFT}\left(\frac{\mathrm{FFT}(\bar{\mathbf{k}}).*\mathrm{FFT}(\mathbf{g})}{\mathrm{FFT}(\bar{\mathbf{k}}).*\mathrm{FFT}(\mathbf{k}) + \lambda\mathcal{I}_\Lambda}\right), \tag{38}$$

where IFFT stands for the two-dimensional inverse FFT.

Various methods can be applied for the estimation of the optimal parameter λ in (38). For details, see [10]. We suggest λ that are obtained from the optimization of (38) for periodic boundary condition satisfying images as regularization parameters for FBCWP for general images. This suggestion produced $\lambda = 0.00098, 0.00069$, and 0.00139 for uniform, Gaussian, and diagonal gradient deblurring simulations in

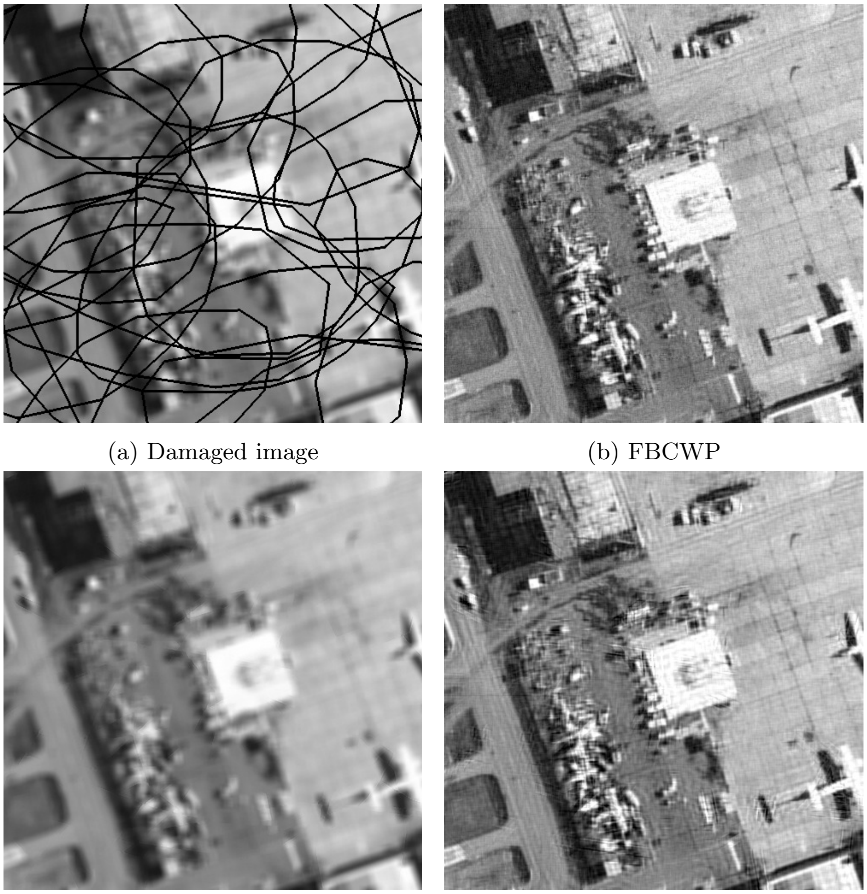
(a) Damaged image

(b) FBCWP

(c) Median filtering

(d) Median filtering + FBCWP

Figure 18. (a) The damaged version of the observed image in Figure 4(b). (b) The deblurred image by FBCWP from the damaged image, by regarding the damaged part, represented by black colored pixels in (a), as part of unseen image pixels across the boundary, i.e., the damaged image in (a) has non-rectangular inner boundaries. (c) The image obtained by applying three-round 3×3 median filtering on the damaged image in (a). Here the median filtering is applied to the image pixel that is not determined in the previous round due to the absence of determined image pixels in 3×3 neighborhood. The median filtered image looks almost identical to the image in Figure 4(b). (d) The deblurred image by FBCWP from the median filtered image in (c). The comparison with the image in (b) shows that a small difference made by mis-filling in median filtering causes severe artifacts in deblurring.

Sections 4.2.1, 4.2.2, and 4.2.3, respectively. These parameters were slightly smaller than near-optimal regularization parameters that were computed by the bisection method. See Figure 13.

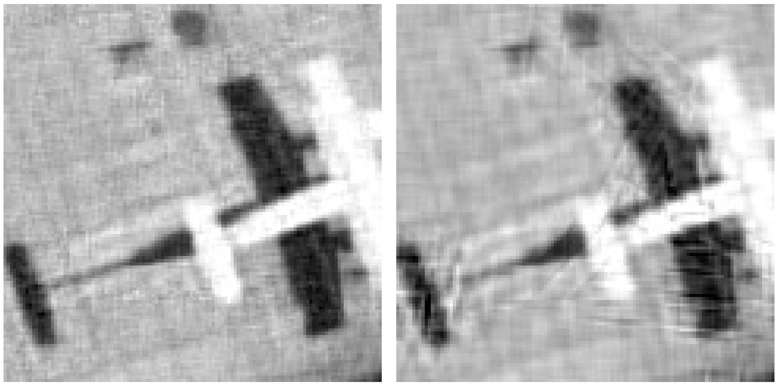

(a) FBCWP (b) Median filtering + FBCWP

Figure 19. (a) A part of Figure 18(b). (b) A part of Figure 18(d).

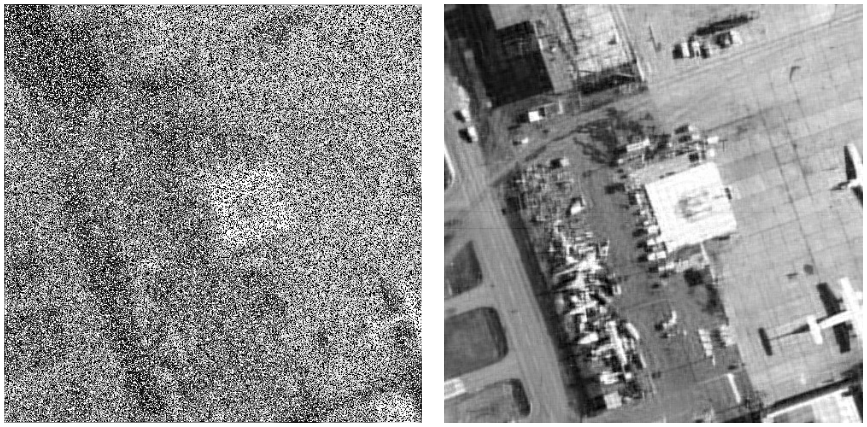

(a) Corrupted by salt-and-pepper noise (b) FBCWP

Figure 20. (a) The observed image $\mathbf{g}$, which is blurred by a 11×11 uniform PSF, and corrupted by “salt and pepper” noise, where 60% of pixels change to the darkest or brightest pixels. In other words, the Gaussian noise in Figure 4(b) is replaced by salt and pepper noise here. (b) The deblurred image by FBCWP from the heavily noised image in (a), by ignoring heavily noised image pixels. FBCWP deblurred the image with RSE = 1.0% at the 99-th iteration. The deblurred image is compatible with the image in Figure 5(d), even though the former only use 40% of the pixel data that is used in the latter.

4.4. **Effect of preconditioning.** In this section we will conduct deblurring by free boundary condition based methods, FBC, FBCW, FBCP, and FBCWP. The purpose of this simulation is to compare the contribution of the preconditioner $\mathcal{W}$ with that of the regularization by the weighted norm $L^2(\Omega, \mathbf{w})$ in removing boundary artifacts. For this purpose, in Figure 16, we present deblurred images on Ω, not on Λ.

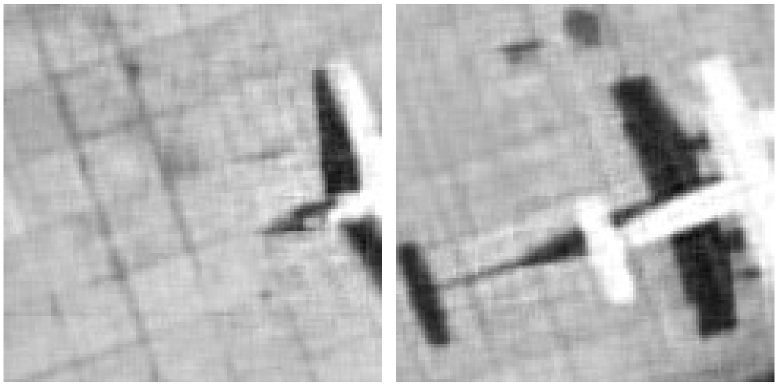

(a) FBCWP (to be compared with Figure 6)

(b) FBCWP (to be compared with Figure 19)

Figure 21. Parts of Figure 20(b), which is deblurred by FBCWP from the "salt-and-pepper" noised image in Figure 20(a). (a) The comparison with images in Figure 6 shows that FBCWP can deblur the images using only 40% of the observed pixels. (b) The comparison with images in Figure 18 shows that FBCWP can deblur the images using only 40% of the observed pixels.

Figure 16 shows deblurred images by FBC, FBCW, FBCP, and FBCWP with $\lambda = 0.001$, from Figure 10 (blurred by the 11×11 diagonal gradient PSF). Here note that the deblurred images in Figure 16 have 'black colored pixels' in lower-left and upper-right corners. Those black colored pixels do not give any contribution to the observation through the 11×11 diagonal gradient PSF, and hence they are not included in Ω.

In Figure 16, the comparison of FBCW with FBC shows that the use of the weighted norm $L^2(\Omega, \mathbf{w})$ does not make noticeable difference in removing boundary artifacts. The comparison of FBCWP with FBCW supports our earlier claim that FBCW and FBCWP produce different results, even though they are based on two equivalent linear systems (9) and (11), due to incomplete CG iterations in FBCW and FBCWP.

Notice that FBCP and FBCWP are preconditioned versions of FBC and FBCW, respectively, by $\mathcal{W}$. In Figure 16, the comparisons between FBC and FBCP, and FBCW and FBCWP show that the use of the preconditioner $\mathcal{W}$ removes boundary artifacts. The visual comparison between FBCP and FBCWP (for better visual comparison, see Figure 17) shows that, even though the effect is not very noticeable in recovering image pixels on Λ, the use of the weighted norm $L^2(\Omega, \mathbf{w})$ helps FBCWP to remove boundary artifacts on $\Omega - \Lambda$ more efficiently than FBCP.

4.5. **Applications of free boundary conditions.** As mentioned in Section 3.1, the proposed method, FBCWP, can be used for arbitrarily-shaped images and it can recover unseen image pixels across the boundary. Combining these two advantages, we can apply FBCWP to other interesting applications in image deblurring.

In this paper, we consider the recovery of damaged parts in noisy blurred images as an application of FBCWP. Let $\mathbf{g}$ be a damaged version, as seen in Figure 18(a), of the noisy blurred image in Figure 4(b), i.e., the true image is sequentially corrupted by 11 × 11 uniform blurring, Gaussian noise $\mathbf{n}$ in (36), and damage. With the assumption that the damaged parts in Figure 18(a) are relatively small so that every image pixel in the damaged parts gives some contribution to our observation, we can use FBCWP to recover image pixels in the damaged parts by treating them as unseen image pixels across the boundary. Figure 18(b) shows the recovered image by FBCWP.

This approach is different from methods that are commonly used in so called *inpainting* applications, in which image pixels in damaged parts are filled up possibly by applying a smoothing transform that resembles a diffusion process [4]. On the other hand, FBCWP treats damaged parts as unseen image parts and recovers them, as a result of deblurring, by using the hidden information (of damaged parts) in undamaged image pixels through blurring.

RBC and ABC cannot be applied to this problem, since RBC and ABC are virtually limited to rectangular images only, and they do not attempt to recover unseen image pixels across the boundary. Another possible approach might take the process of recovering damaged image pixels first and the processing of deblurring after that. Figure 18(c) shows the result of recovering damaged image pixels by applying three-round 3 × 3 median filtering on Figure 18(a), and Figure 18(d) shows the result of deblurring by FBCWP from Figure 18(c). Even though Figure 18(c) is almost identical to Figure 4(b), Figure 18(d), deblurred from Figure 18(c), suffers from artifacts all over the image, while Figure 18(b), directly deblurred from Figure 18(a), does not show any noticeable artifacts. Zoomed images in Figure 19 show detailed comparisons.

The success of FBCWP in the recovery of damaged pixels can be extended to image recovery in the presence of 'salt and pepper' noise. Figure 20(a) shows the observed image, which is blurred by 11 × 11 uniform PSF, and corrupted by salt and pepper noise, where randomly selected 60% of the image pixels change to black or white pixels. In other words, the Gaussian noise in Figure 4(b) is replaced by salt and pepper noise in Figure 17(a). Figure 20(b) shows the deblurred image by FBCWP from Figure 20(a), by regarding salt and pepper noised image pixels, which can be easily detectable by checking intensities at image pixels, as unseen image pixels across the boundary. Figure 20(b) was obtained at the iteration 99 with RSE = 1.0%. This result is compatible with the result in Figure 5(d), which is obtained at iteration 53 with RSE = 0.98%, even though Figure 20(b) used only 40% of of the pixels in the observed image. Zoomed images in Figure 21 show detailed comparisons.

5. **Conclusion and discussion.**

In this paper we propose using free boundary conditions, which do not impose any restrictions on unseen image pixels, and the preconditioned CG method, where the preconditioner is designed to compensate for the non-uniformity in contributions from image pixels to the observation, in image deblurring. In simulation studies with uniform, Gaussian, and diagonal gradient PSFs, the proposed method, FBCWP, outperforms RBC (the reflective boundary condition–based CG method) and ABC (the anti-reflective boundary condition–based CG method) in all test images objectively, by having smaller RSE, and subjectively, by not showing boundary artifacts. Simulation results in Section 4.5 show that FBCWP can be used for the recovery of damaged regions in noisy blurred images by treating damaged regions as unseen image pixels across the boundary. Based on these simulation results, we can conclude that FBCWP is more efficient in removing boundary artifacts, more flexible in dealing with boundaries, and more applicable in image deblurring than RBC and ABC.

As mentioned earlier, methods in [6, 2] also use free boundary conditions. To be specific, the method proposed in [6] has the form of FBCW (incomplete CG iteration applied to $(\mathcal{T}^*\mathcal{T}+\lambda\mathcal{W})\mathbf{p} = \mathcal{T}^*\mathbf{g}$) if $\mathcal{W}$ is replaced with the Laplacian operator. Thus, the main difference between the proposed method FBCWP and the method in [6] lies in the use of preconditioner $\mathcal{W}$ and the choice of the Tikhonov regularization. On the other hand, the method in [2] applies the free boundary condition in alternating direction method of multipliers (ADMM) for image deblurring. Therefore, the main difference between the method in [2] and the proposed method FBCWP lies iterative methods; the former uses ADMM and the latter uses preconditioned CG iterations.

Simulation results in this paper show that the non-uniformity in contributions from image pixels to the observation, instead of the existence of unseen image pixels across the boundary, is the main source of boundary artifacts in image deblurring. Therefore, the use of the preconditioner $\mathcal{W}$ (34) exactly as suggested in FBCWP is an essential step in removing boundary artifacts.

The non-negativity of the PSF is an essential requirement for the success of FBPWP. For example, if the PSF is not non-negative, then the preconditioner $\mathcal{W}$ (34) may not be defined, since the weight $(\mathcal{T}^*\mathbf{I}_\Lambda)_{i_1,i_2}$ in (33) could be zero for some image pixel (i_1, i_2). This would violate the invertibility of the preconditioner $\mathcal{W}$ in (34).

Acknowledgments. The work of the first author was supported by the Inje Research and Scholarship Foundation in 2012 and conducted while the first author was a visiting scholar at the Center for Nonlinear Analysis, Department of Mathematical Sciences, Carnegie Mellon University. The work of the second author was supported in part by grants from the Simons Foundation (Awards #209418 and #229816).

REFERENCES

[1] F. Aghdasi and R. K. Ward, Reduction of boundary artifacts in image restoration, *IEEE Trans. Image Processing*, **5** (1996), 611–618.

[2] M. S. C. Almeida and M. A. T. Figueiredo, Frame-based image deblurring with unknown boundary conditions using the alternating direction method of multipliers, in *Proceedings of ICIP*, (2013), 582–585.

[3] A. Arićo, M. Donatelli and S. Serra-Capizzano, Spectral analysis of the anti-reflective algebra, *Linear Algebra Appl.*, **428** (2008), 657–675.

[4] M. Bertalmio, G. Sapiro, V. Caselles and C. Ballester, Image inpainting, *SIGGRAPH*, (2000), 417–424.

[5] M. Bertero and P. Boccacci, A simple method for the reduction of boundary effects in the Richardson-Lucy approach to image deconvolution, *Astron. Astrophys.*, **437** (2005), 369–374.

[6] D. Calvetti, J. P. Kaipio and E. Someralo, Aristotelian prior boundary conditions, *Inter. J. Mathematics and Computer Science*, **1** (2006), 63–81.

[7] M. Donatelli, C. Estatico, A. Martinelli and S. Serra-Capizzano, Improved image deblurring with anti-reflective boundary conditions and re-blurring, *Inverse Problems*, **22** (2006), 2035–2053.

[8] Y. W. Fan and J. G. Nagy, Synthetic boundary conditions for image deblurring, *Linear Algebra Appl.*, **434** (2011), 2244–2268.

[9] C. W. Groetsch, *The Theory of Tikhonov Regularization for Fredholm Integral Equations of the First Kind*, Pitman, Boston, 1984.

[10] M. Hanke and P. C. Hansen, Regularization methods for large-scale problems, *Surveys Math. Indust.*, **3** (1993), 253–315.

[11] M. R. Hestenes and E. Stiefel, Methods of conjugate gradients for solving linear systems, *Journal of Research of the National Bureau of Standards*, **49** (1952), 409–436.

[12] A. K. Jain, *Fundamentals of Digital Image Processing*, Prentice-Hall, Englewood Cliffs, NJ, 1989.

[13] R. Liu and J. Jia, Reducing boundary artifacts in image deconvolution, in *Proceedings of ICIP*, 2008, 505–508.

[14] L. B. Lucy, An iterative techniques for the rectification of observed distributions, *Astronomical Journal*, **79** (1974), 745–754.

[15] M. K. Ng, R. H. Chan and W.-C. Tang, A fast algorithm for deblurring models with Neumann boundary conditions, *SIAM J. Sci. Comput.*, **21** (1999), 851–866.

[16] W. H. Richardson, Bayesian-based iterative method of image restoration, *J. Opt. Soc. Am.*, **62** (1972), 55–59.

[17] Y. Saad, *Iterative Methods for Sparse Linear Systems*, SIAM Publications, Philadelphia, 2003.

[18] S. Serra-Capizzano, A note on anti-reflective boundary conditions and fast deblurring models, *SIAM J. Sci. Comput.*, **25** (2003), 1307–1325.

[19] A. M. Tekalp and M. I. Sezan, Quantitative analysis of artifacts in linear space-invariant image restoration, *Multidimensional Syst. Signal Processing*, **1** (1990), 143–177.

[20] R. Vio, J. Bardsley, M. Donatelli and W. Wamsteker, Dealing with edge effects least-squares image deconvolution problems, *Astron. Astrophys*, **442** (2005), 397–403.

[21] J. W. Woods, J. Biemond and A. M. Kekalp, Boundary value problem in image restoration, *Proc. Sixth Int. Conf. Acoust. Speech Signal Processing*, **10** (1985), 692–695.

Received May 2013; revised September 2015.

E-mail address: nylee@inje.ac.kr
E-mail address: lucier@math.purdue.edu